NUMERICAL STUDY OF ARC EXPOSURE ABOUT WATER-PANEL OVERHEATING IN AN ELECTRIC ARC FURNACE

by

Qingxuan Luo

A Thesis

Submitted to the Faculty of Purdue University

In Partial Fulfillment of the Requirements for the degree of

Master of Science in Mechanical Engineering

Department of Mechanical and Civil Engineering

Hammond, Indiana

December 2021

THE PURDUE UNIVERSITY GRADUATE SCHOOL
STATEMENT OF COMMITTEE APPROVAL

Dr. Chenn Q. Zhou, Chair

Department of Mechanical and Civil Engineering

Dr. Xiuling Wang

Department of Mechanical and Civil Engineering

Dr. Ran Zhou

Department of Mechanical and Civil Engineering

Approved by:

Dr. Xiuling Wang

To my parents

ACKNOWLEDGMENTS

First of all, I would like to say thanks to my advisor, Prof. Chenn Q. Zhou for her invaluable guidance and meticulous concern over the past two and a half years. It was Chenn Q. Zhou who offered me the opportunity to work as a student worker in the Center for Innovation through Visualization and Simulation (CIVS). She taught me a lot of knowledge about my research and encouraged me to walk out from confusion. I would also like to say thanks to Prof. Xiuling Wang and Prof. Ran Zhou for joining my advisory committee and providing precious comments for me.

Besides, I would like to express my appreciation to my colleagues at the Center for Innovation through Visualization and Simulation (CIVS) at Purdue University Northwest and all committee members from the Steel Manufacturing Simulation and Visualization Consortium (SMSVC) for their invaluable support of this project. Dr. Armin Silaen, Dr. Tyamo Okosun, Mr. Yu Wang, Mr. Haibo Ma, Mr. Xipeng Guo, Mr. Congshan Mao, Mr. Neel Busa and many others in CIVS, I want to express my sincere thanks to them. I would like to say thanks Dr. Sunday Abraham and Dr. Yufeng Wang from SSAB company for the project and support data. Especially, I would like to appreciate Mr Yuchao Chen for his invaluable and patient guidance during these two and a half years.

Finally, I want to express my thanks to my family and my friends. Any words would be too weak to express my parents’ commitment to me. A special appreciation is for my friend, Mr. Xiang Li, sharing of pleasure, anger, sorrow and joy with him really supported me during these years in this foreign country.

TABLE OF CONTENTS

LIST OF TABLES

LIST OF FIGURES

NOMENCLATURE

Symbol	Description	Symbol	Description
U	Arc voltage	I	Arc current
ρ_a	Arc resistivity	j_k	Arc resistivity
r_k	Cathode-spot current density	r_a	Arc radius
z	Axial distance from cathode	$L_{A,e}$	Exposed arc length
$L_{A,t}$	Total arc length	H_f	Foaming height
P	Arc power	P_r	Radiation arc power
r_k	Cathode-spot radius	v_g	Superficial velocity
Σ	Foaming index	μ_s	Slag viscosity
σ_s	Slag surface tension	ρ_s	Slag density
X_i	Mole fraction of species	T	Temperature
ρ	Density	τ	Stress tensor
ρg	Gravitational body force	F	External body force
k_{eff}	Effective thermal conductivity	J	Diffusion flux
Pr_t	Turbulent Prandtl number	S_h	Heat of chemical reaction
E	Total energy	h	Sensible enthalpy
c_p	Specific heat	k	Turbulent kinetic energy
ε	Turbulence dissipation rate	μ	Viscosity
μ_t	Turbulent viscosity	M_τ	Turbulent Mach number
σ_k	1.0	σ_ε	1.3
$C_{\varepsilon 1}$	1.44	$C_{\varepsilon 2}$	1.92
a	Acoustic velocity	T_g	Normalized local total temperature gradient
T_t	Local total temperature	$H(x)$	Heaviside function
$M_{\tau 0}$	0.1	ω	Specific dissipation rate
G_k	Production of k	G_ω	Generation of ω
Γ_k	Effective diffusivity of k	Γ_ω	Effective diffusivity of ω

Y_k	Dissipation of k due to turbulence	Y_ω	Dissipation of ω due to turbulence
D_ω	Cross-diffusion term	q_r	Radiation flux
Y_i	Mass fraction of species i	J_i	Diffusion flux term of species i
R_i	Net rate of production of species i	$D_{i,m}$	Diffusivity for species i
Sc_t	Turbulent Schmidt number	$D_{T,i}$	Thermal diffusion coefficient

ABSTRACT

Electric arc furnace (EAF) is a furnace that utilizes electric energy and chemical energy to melt scraps and produce liquid steel. During the industrial process of EAF, an electric arc will be generated around the electrode located at the center of the furnace, and this phenomenon will generate a lot of heat. If any part of the electric arc is exposed to the freeboard region, a region above the slag layer inside the furnace, the heat emitted by this exposed arc can significantly heat on side wall temperatures, resulting in an overheating issue of side wall. Water-cooling panels (WCP) have been used to cool down the side wall, but the concentrated overheating area, may damage the water-cooling panel. In this study, a combination of slag foaming phenomenon and electric arc has been considered. A calculator is developed based on several arc models to calculate the parameters about slag foaming and arc power. The parameters can be used as input in a computational fluid dynamics (CFD) model. The commercial software, ANSYS FLUENT®, was utilized to give a prediction of the side wall temperature distribution of an EAF. Data from the plant has been used to validate the calculation results. Furthermore, a series of parametric studies has been investigated to study the influence of operating conditions. The developed model can help to predict the risk of overheating from given electrode conditions and slag compositions.

1. INTRODUCTION

1.1 Electric Arc Furnace in Steelmaking

An electric arc furnace (EAF) is a furnace that utilizes electric energy and chemical energy to melt scraps and to produce steel. EAF has been widely used in worldwide to produce about 28% of the steel in the world and has produced about 67% steel in North America in 2019 [1]. EAF now makes an important role in the steelmaking industry. As illustrated in Figure 1.1, 83.8 million metric tons of crude steel has been produced in the US in 2018, and EAF production makes up 67% of it [2]. During the past years, EAF share is growing, meaning that EAF is more and more important in US steelmaking.

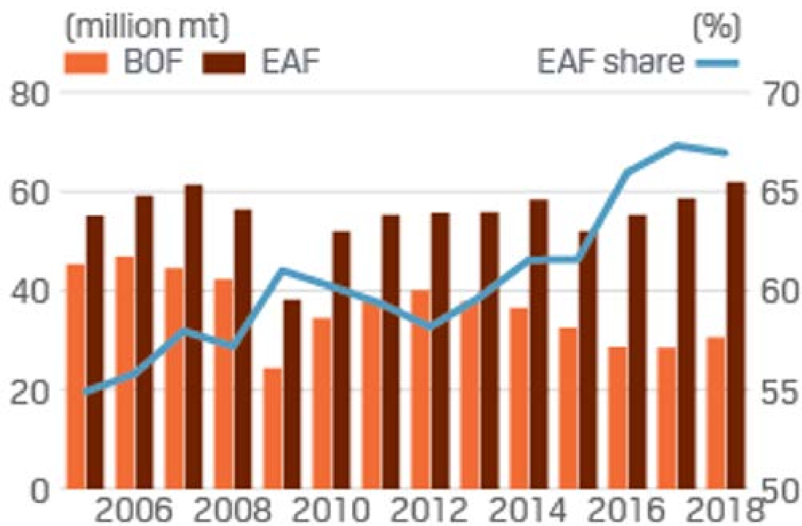

Figure 1.1 EAF steelmaking share in US. [2]

Figure 1.2 shows the structure of a typical DC EAF [3]. A single upper electrode is installed at the central top of EAF. A central electric arc can be produced between the upper electrode and the bottom electrode. The roof and the side wall of the furnace, called shell, are covered by panel, water will be used to cool down these parts during the industrial process. Several burners installed on the side of the furnace; jets will be injected through these burners to help refine the steel. An outlet locates at the bottom of the side will let liquid steel pass through at the end of EAF process.

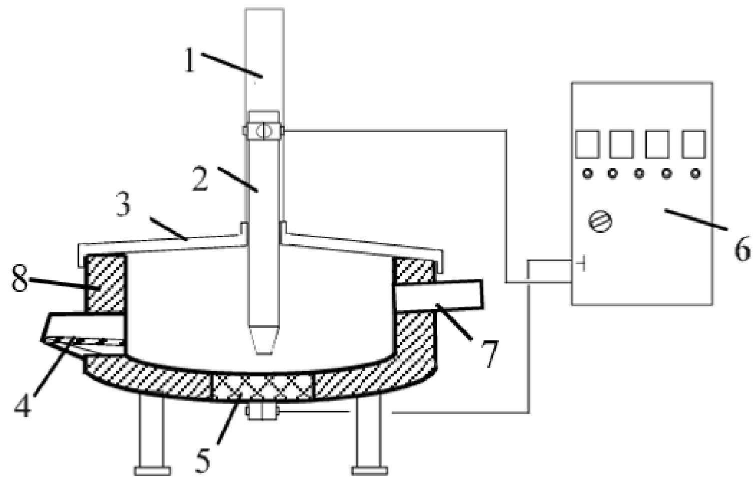

1 – Bracket 2 – Top electrode (Cathode) 3 – Water cooled roof
4 – Outlet 5 – Bottom electrode (Anode) 6 – DC electrical source
7 – Burner 8 – Water cooled shell

Figure 1.2 A typical DC electric arc furnace structure. [3]

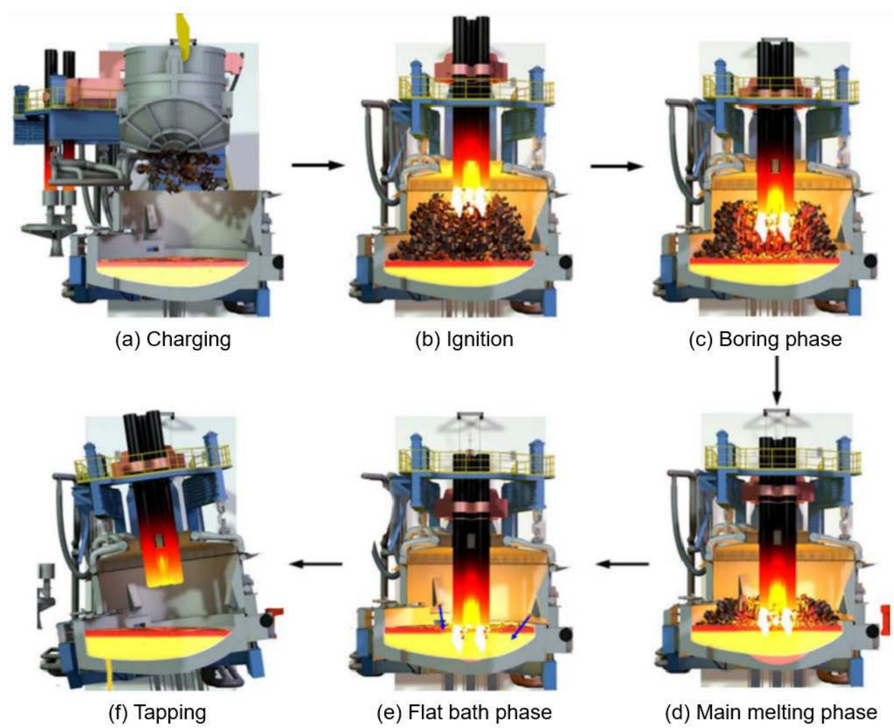

Figure 1.3 A typical AC EAF process [4].

A typical AC EAF process is shown in Figure 1.3 [4]. Compared to DC EAF, an AC EAF would substitute 3 electrodes to the single electrode at the top. At the beginning of charging process, electrodes move away from the furnace, and a basket carrying scraps move to the position above the furnace to charge the scraps from the top of furnace. In melting process, electrodes are moved back and inserted into the furnace so as to produce electric arc. The huge heat generated by electric arc will melt any scrap contacted to the electric arc. As long as electrodes moving deeper into the furnace, the scrap will be bored until electrodes are moved to the bottom and kept at this position. A cavity around the electrodes will grow bigger, and the rest scraps will not be able to support the pile, and collapse down. The bottom of the furnace will be covered by steel in liquid. After the scraps are melted, the refining process begins. Several oxygen jets are injected through the burners to help melt, stir and oxidize elements in the liquid steel. At the end of the EAF process, the EAF will be inclined and the liquid steel will be tapped out through the tapping hole.

1.2 EAF Freeboard Post-Combustion

During the industrial process of EAF, several jets composed by fuel and oxygen are be injected through burners installed on the side wall of the furnace [5]. These jets can help melt the scraps far from the central electrodes where heat may be difficult to be transferred to, and these jets can also help stir the liquid bath. As shown in Figure 1.4, there are two types of supersonic jets used in industry: conventional jet and coherent jet. In previous years, industries may use conventional jets, which has only a central oxygen jet, but this type of jet may be influenced by the high temperature vortex inside the furnace and may not travel a long distance. The supersonic coherent jet is composed by a central oxygen jet as well as a series of fuel jets and extra oxygen jets around the center oxygen jet to form a flame envelope, so as to help protect the central supersonic jet and provide some heat to help melt the scraps. In this project, the supersonic coherent jet is considered to give an accurate prediction of the flow field inside the furnace.

During refining process, the injected oxygen through burners can oxidize some elements like silicon, aluminum, and manganese, will generate a slag layer [6]:

$$Si + O_2 = SiO_2 \tag{1}$$

$$Al + \frac{3}{4}O_2 = \frac{1}{2}Al_2O_3 \tag{2}$$

$$Mn + \frac{1}{2}O_2 = MnO \tag{3}$$

To reduce the iron element in the slag layer, some carbon will be charged with the original scraps, and some may be injected during the refining process. Reduction reaction of carbon with FeO in the slag will produce carbon monoxide gas [6]:

$$C + O_2 = CO_2(g) \tag{4}$$

$$Fe + \frac{1}{2}O_2 = FeO \tag{5}$$

$$FeO + C = Fe + CO(g) \tag{6}$$

The generated CO gas will react with the injected O_2 in the zone above the slag bath, called freeboard. The phenomenon of combustion between CO and O_2 is the freeboard post-combustion phenomenon.

With the gas foaming from the bottom bath, and a slag layer to sustain the gas in shape of bubble, the slag foaming phenomenon will take place continuously. Appearance of the slag foaming phenomenon can help block the huge radiation heat from central electric arc. Figure 1.5 shows the slag foaming phenomenon [7].

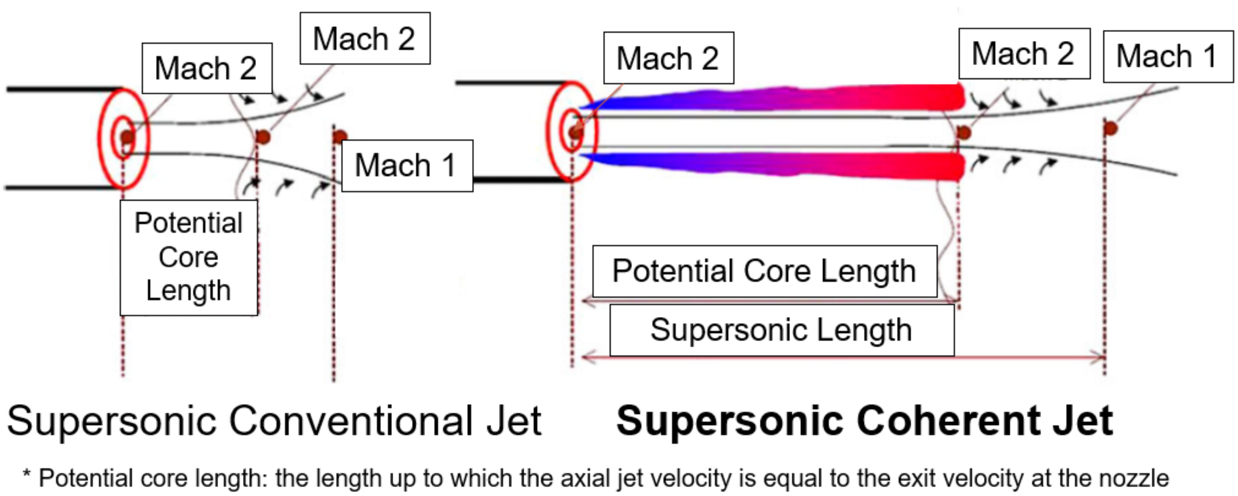

Figure 1.4 Supersonic conventional jet and supersonic coherent jet [5].

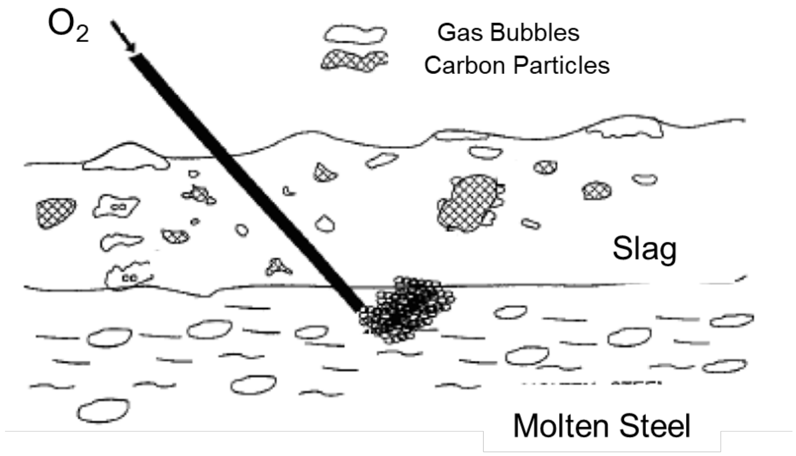

Figure 1.5. Slag foaming phenomenon.

1.3 Water-Cooling Panel Overheating Issue

In refining stage, the electric arc exposed to the part above the liquid bath, or called freeboard, can significantly heat up the wall of furnace. In general, higher operating temperature means high power to melt and refine the scraps more quickly, so that the productivity will be increased. On the other hand, the significant electric energy can also damage the furnace wall because of the high temperature. To reduce the overheating, water cooling panels (WCP) are installed on the side wall and the roof to cool down the overheated wall by water. However, high temperature may still concentrate on the certain area on the EAF shell, called hot spot. The hot spot may overheat the WCP and make it perforated, which could lead to serious results like explosion. In recent years, sensors have been set up to monitor the condition of cooling water and alarms will be triggered if the excessive temperature appears. so that steelmaking industries can take issues, like reducing arc power reasonably to control the WCP temperature.

As a main energy source of EAF, electric arc takes up about 45% to 65% of the total energy. Arc power is delivered in 3 different forms: convection, radiation and electron flow. Among these 3 ways, extremely high temperature of the arc makes the share of radiation can be up to about 34% to 80% according to researchers [8]. Once the electric arc is exposed to the furnace walls, the huge power brought by electric arc in form of radiation can heat up these walls, leading to the excessive temperature on the water panels, and WCP overheating issue will appear. This is also an important reason why industries may take reducing the electric arc power as an approach to reduce the overheating issue.

The slag foaming phenomenon is effective to protect the side wall from being heated up by the exposed electric arc. The covered electric arc will deliver most of the energy to slag layer and liquid steel rather than emitting heat to the furnace shell. To obtain a scheme to reduce the WCP overheating issue, it is applicable to find out a detailed relationship of slag foaming phenomenon with arc exposure and WCP overheating issue. In this paper, both mathematic and computational fluid dynamics (CFD) methods have been used.

1.4 Objective

In this article, an arc exposure calculator has been developed to calculate the parameters for arc conditions and slag foaming conditions. A computational fluid dynamics (CFD) model has been developed to give a prediction of side wall temperature distribution of an industrial EAF, so as to predict the overheating risk of the condition. The primary objectives of this research are about:

1. To develop a slag foaming model to give a prediction of slag foaming conditions based on industrial operating data.

2. To develop a comprehensive CFD simulator including a geometry and related mesh of an industrial DC electric arc furnace to illustrate the performance of the calculated results.

3. To conduct a model validation by comparing the simulation results with the industrial data so as to prove the accuracy of developed model.

4. To conduct a series of parametric studies to investigate the influence of parameters on overheating issue and give related advice to reduce the overheating in industrial process.

2. LITERATURE REVIEW

2.1 Supersonic Coherent Jet

In recent years, researchers have studied the supersonic coherent jet in numerical method [9][10][11]. In 2019, Tang and Chen et al. developed a CFD model to simulate the supersonic coherent jet of an EAF [10]. Their simulation domain has been shown in Figure 2.1, considering a central supersonic oxygen jet, shrouded fuel jet and secondary oxygen jets. Eddy-dissipation concept (EDC) model was used to calculate the combustion between methane as the fuel and oxygen. Discrete-ordinates (DO) radiation model and a modified Weighted-Sum-of-Gray-Gases Model (WSGGM) was used to calculate the radiation heat transfer between the gas species. The simulation results are shown in Figure 2.2. It can be noticed that the coherent jet can keep high speed for a longer distance than the conventional jet because of the protection from flame envelope.

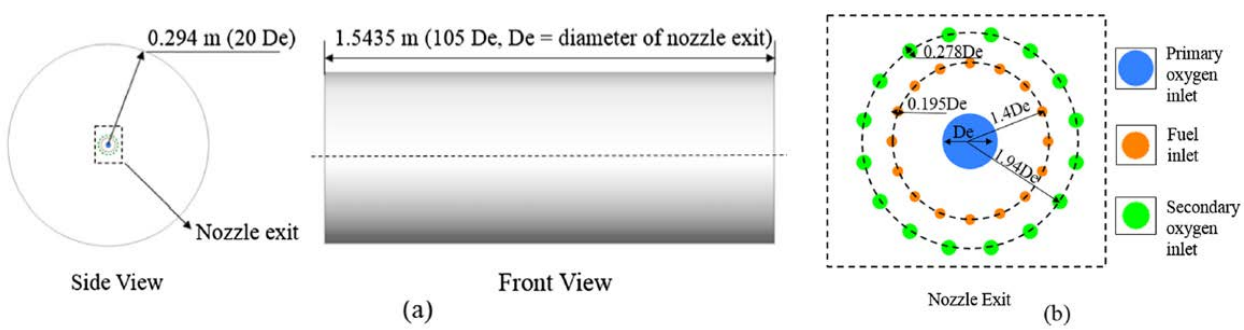

Figure 2.1 Simulation domain of (a) front view and (b) side view [10].

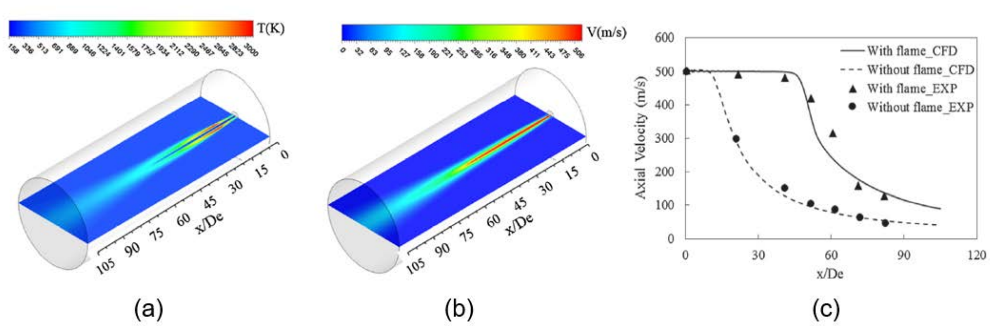

Figure 2.2 Simulation results of (a) temperature contour (b) velocity contour and (c) axial velocity plot with a function of distance [10].

2.2 DC Electric Arc

In a DC arc furnace, the electric arc is usually generated between a single graphite cathode and a metal bath at the bottom of a furnace inner vessel. A DC arc schematic representation is shown in Figure 2.3. The distance from cathode to anode is the electric arc length. In industry, electric arc power can be determined by both electric arc length and arc current. It is necessary to obtain an accurate prediction of the arc voltage based on the electrode conditions including arc length and arc current.

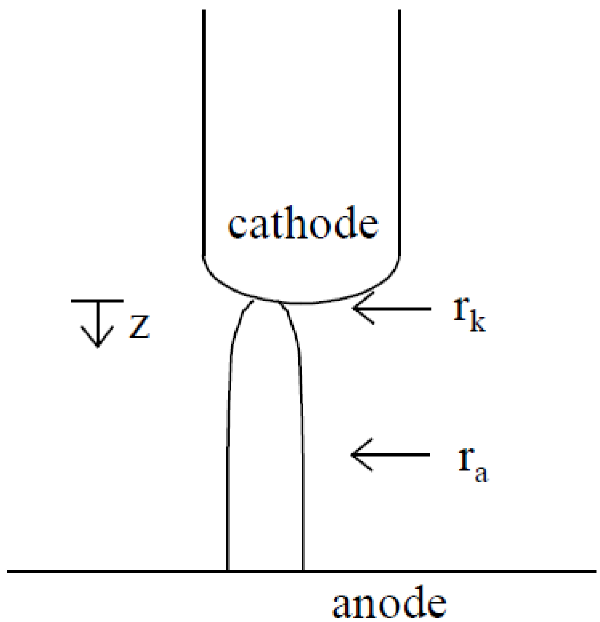

Figure 2.3 Schematic representation of a DC arc [12].

In 2002, Jones et al [12] integrated an equation based on Bowman's research [13] about the calculation of voltage based on current and the distance from cathode:

$$U = \rho_a \cdot \sqrt{\frac{Ij_k}{\pi}} \cdot \int (\frac{r_k}{r_a})^2 dZ \tag{7}$$

$$Z = \frac{z}{r_k} \tag{8}$$

Where U, I, ρ_a, j_k, r_k, r_a, z, are voltage in V, current in A, arc resistivity in Ωcm , cathode-spot current density in kA/cm^2, cathode-spot radius in cm, arc radius in cm and axial distance from cathode in cm, respectively.

Jones finished the integration and obtained an equation to express the relationship of arc voltage, current and arc length:

$$U = \frac{I\rho_a}{m\pi}\left[-\frac{1}{a^2+ab}+\frac{1}{a^2+ab\cdot\exp{(mL)}}+\frac{\ln{(a+b)}}{a^2}+\frac{mL}{a^2}-\frac{\ln{[a+b\cdot\exp(mL)]}}{a^2}\right] \tag{9}$$

$$a = 3.2\, r_k \tag{9a}$$

$$b = -2.2\, r_k \tag{9b}$$

$$m = \frac{-1}{5r_k} \tag{9c}$$

$$r_k = \sqrt{\frac{I}{\pi(3500A/cm^2)}} \tag{9d}$$

Where L is arc length in cm. Figure 2.4 shows the calculated voltage of this equation with a function of arc length for a range of different arc currents at a given value of arc resistivity of 0.014 Ωcm.

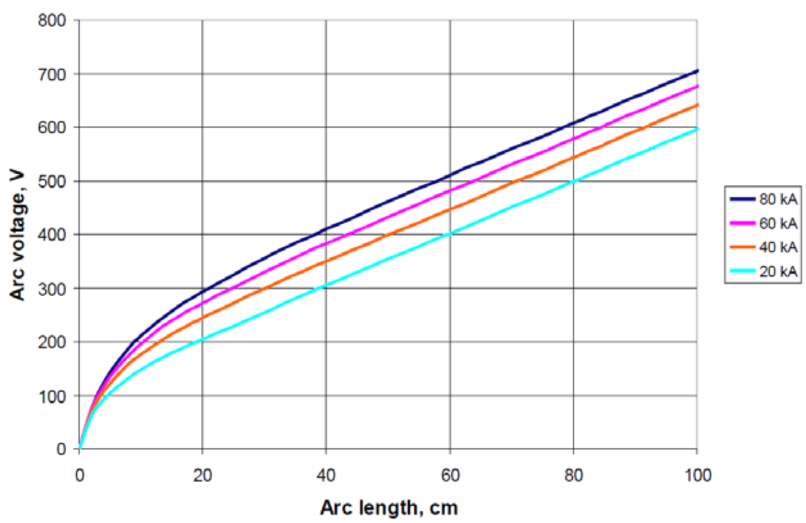

Figure 2.4 Arc voltage as a function of arc length at different currents, for a given arc resistivity of 0.014 Ωcm [12].

Jones' work revealed the relationship of DC arc length, arc voltage and current, which can be used for the calculation of arc length from arc voltage and current reversely.

2.3 Slag Foaming Phenomenon

Slag foaming phenomenon has been studied by many researchers. These authors were focused on the slag foaming height to describe the degree of slag foaming. In 2011, Luz and Pandolfelli reviewed a series of relative researches [7]. Figure 2.5 shows a schematic apparatus to evaluate slag foaming phenomenon for an electric furnace. In this procedure, no chemical reactions were taken into consideration, and only liquid behaviors were considered.

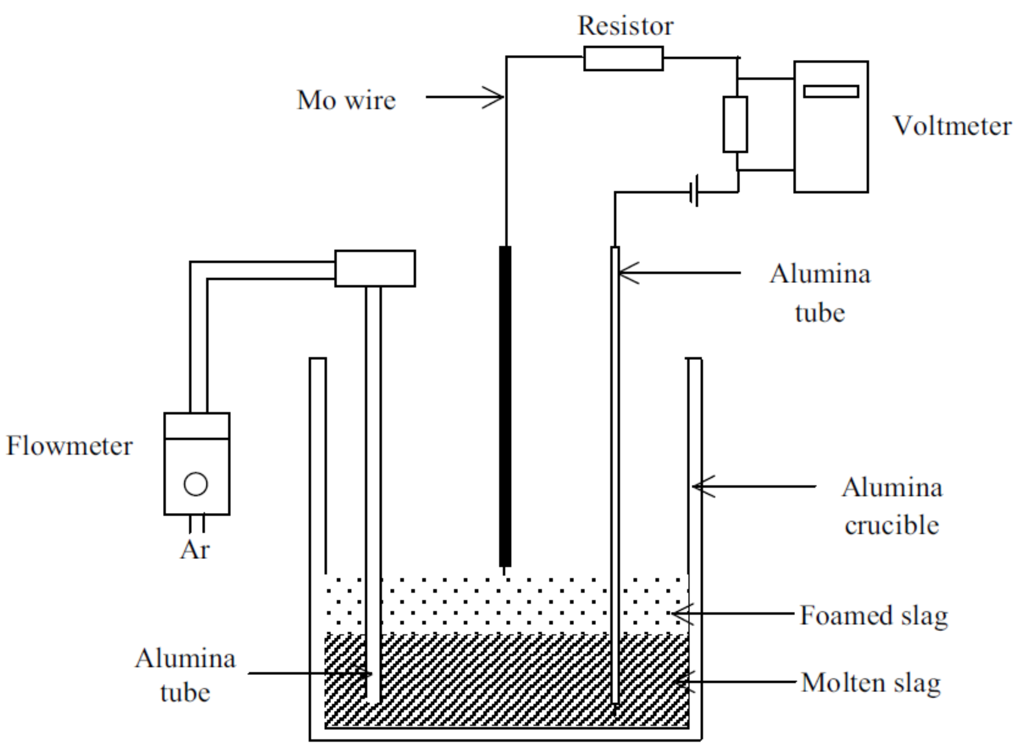

Figure 2.5 An experimental apparatus to measure the slag height when gas is injected into the molten slag [7].

In 1989, Ito and Fruehan raised an equation to calculate out the slag foaming height by foaming index and superficial velocity [14]:

$$H_f = \Sigma \cdot v_g \tag{10}$$

Where H_f, Σ and v_g are foaming height in m, foaming index in s and superficial velocity in m/s. The foaming index is a parameter expressing the average travelling time of the gas in the generated foam is attained. The foaming height is a ratio of foaming height and superficial velocity, it is related to some slag physical properties, such as viscosity, surface tension and density. In Ito and Fruehan's research, an equation to calculate the foaming index of a CaO–SiO_2–FeO–Al_2O_3 has been obtained [15]:

$$\Sigma\ = 570\frac{\mu_s}{\sqrt{\sigma_s\rho_s}} \tag{11}$$

Where μ_s, σ_s, and ρ_s are slag viscosity, slag surface tension and slag density, respectively.

In 1991, Jiang and Fruehan enhanced the model by giving more accurate definition of foaming index [16]. They considered the foaming index in acid slags and basic slags respectively:

$$\Sigma\ = 115\frac{\mu_s}{\sqrt{\sigma_s\rho_s}}\ \text{(For basic slags)} \tag{12}$$

$$\Sigma\ = 0.93\frac{\mu_s}{\sigma_s{\rho_s}^{2/3}}\ \text{(For acid slags)} \tag{13}$$

In 1995, Zhang and Fruehan suggested another expression similar to the Jiang and Fruehan's equation, and also take bubble diameter D_b (m) into consideration [17]:

$$\Sigma\ = 115\frac{{\mu_s}^{1.2}}{{\sigma_s}^{\mathbf{0.2}}\rho_s D_b^{0.9}}\ \text{(For basic slags)} \tag{14}$$

$$\Sigma\ = 1.03\times10^4\frac{{\sigma_s}^{12}}{\mu_s^{0.4}\rho_s^{11.7}D_b^{23}}\ \text{(For acid slags)} \tag{15}$$

The researches above did not consider the relationship of initial slag layer height and the foaming height. In 2010, Wu, Albertsson and Du designed a series of experiments of silicone oil slag foaming to investigate the relationship of initial height and foaming height [18]. Figure 2.6 shows the photographs of oil foams at three different superficial velocities. For foams with low velocity, it can be noticed that many small gas bubbles scatter inside the oil and rise slowly. Increased foam height is little in this situation. When gas superficial velocity is too high, the gas may rise rapidly, the foam cannot be sustained so that increasing of foam is also very little. Only when gas superficial velocity is controlled in a proper range, the bubble can rise properly and the foam can be generated significantly.

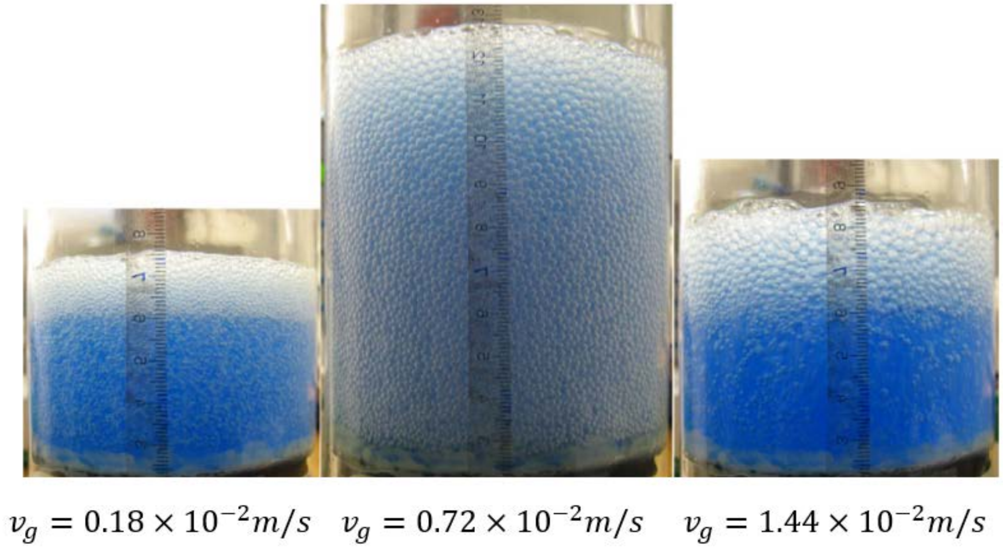

Figure 2.6 Image of slag foaming [18].

Wu et al. concluded an equation with the relationship of increased height Δh and initial height h_0:

$$\frac{\Delta h}{h_0} = 2.238\left(\frac{\nu^4 \rho_s^3 g}{\sigma_s^3}\right)^{0.045} exp\left\{-8150\left[j - (\frac{\nu_0}{\nu})^{\frac{1}{2}} j_0\right]^2\right\} \\ exp\left[-1.094 \times 10^8 (\nu - \nu_0)^2\right] \tag{16}$$

Where ν, ν_0, g, j, j_0 are the kinematic viscosity of the liquid, the kinematic viscosity at which the foaming of the liquid at a given superficial velocity shows a maximum, gravitational acceleration, the superficial velocity of gas and the superficial velocity at which the foaming of the liquid at a given kinematic viscosity shows a maximum, respectively.

In 2009, Matsuura and Fruehan [19] developed a mathematic model, calculated a slag foaming height based on Zhang and Fruehan's work [17] of Equation (14). A series of studies was conducted by Matsuura and Fruehan about weight of scraps and pig iron, weight of slag and input amount of fuel and oxygen. Figure 2.7 shows a group of study about weight of scraps and pig iron. It can be noticed that EAF slag does not vary too much during the operating process, and increasing the amount of scrap will increase the FeO component in the slag. Figure 2.8 shows CO generation rate in different sources and the slag foaming height of the simulation results with or without the consideration to limit the slag amount. It can be noticed that CO generation rate can directly determine the foaming height at the beginning or the end of the process when CO generation rate is low. During the majority of the process, limitation of slag amount makes more difference on the limitation of slag foaming height.

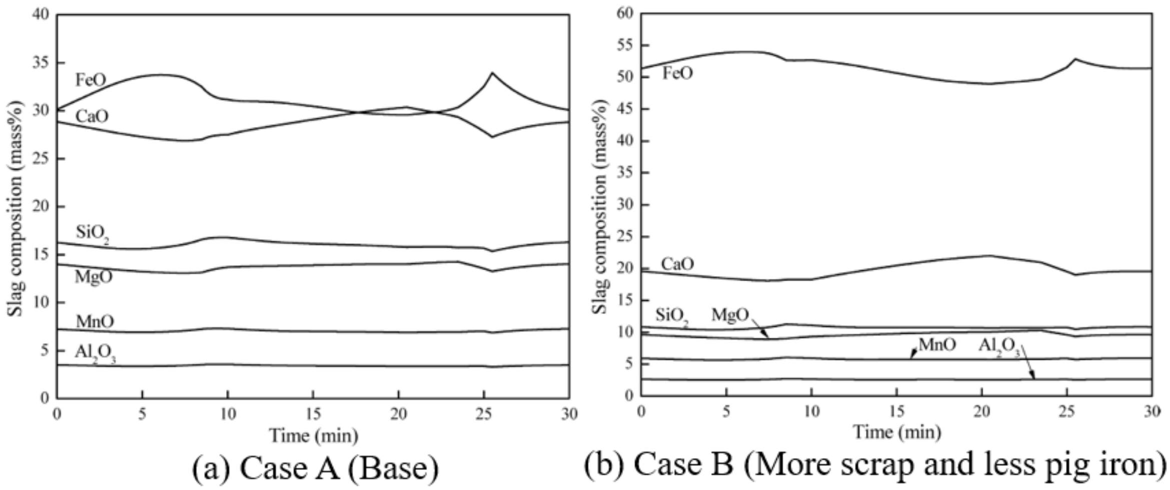

Figure 2.7 Slag compositions with a function of time in different cases [19].

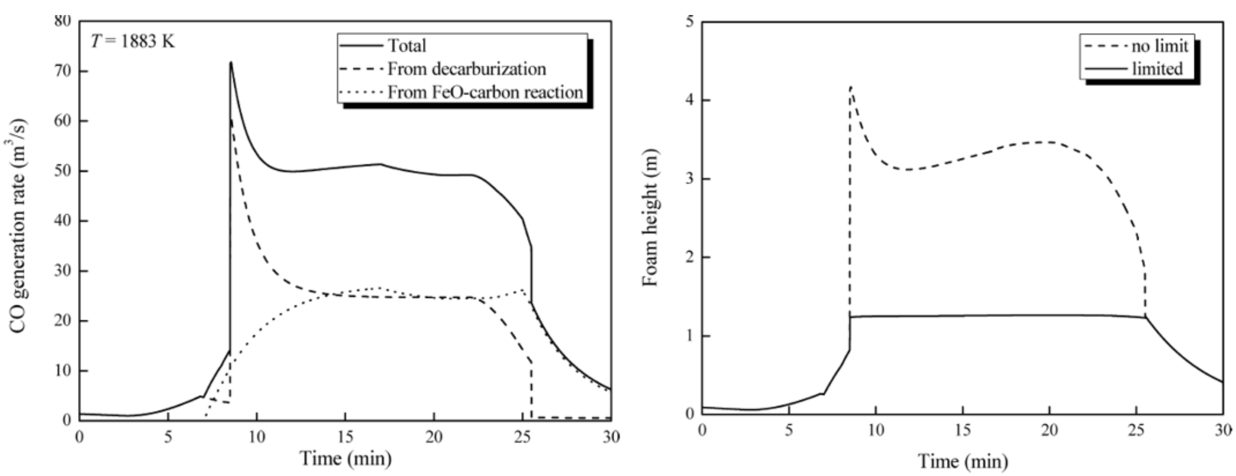

Figure 2.8 Simulation results with a function of time of base case. Left: CO generation rate. Right: Foaming height of base case with or without limitation of slag weight [19].

2.4 Water-cooling Panel Overheating Issue

The free burning arc exposed to the freeboard can lead to a waste of energy and a risk of overheating issue on water-cooling panel. In recent years, researchers have studied the WCP overheating issue in different ways.

Some researchers generated and simulated the structure of water-cooling panels to investigate the heat transfer of panels. In 2017, Khodabandeh et al. developed a cooling system of EAF and simulated the temperature distribution on the panels [20]. As can be seen in Figure 2.9, a series of water-cooling panels were installed outside the wall of this AC EAF. Electric arc would be generated from the central 3 electrodes, and cooling water would flow through the panels. Surface to surface (S2S) radiation model was utilized to simulate the heat transfer from central electric arc to the side wall. As shown in Figure 2.9, this model simulated the temperature distribution of the water-cooling panel, from inlet to outlet, the temperature of cooling water was increased.

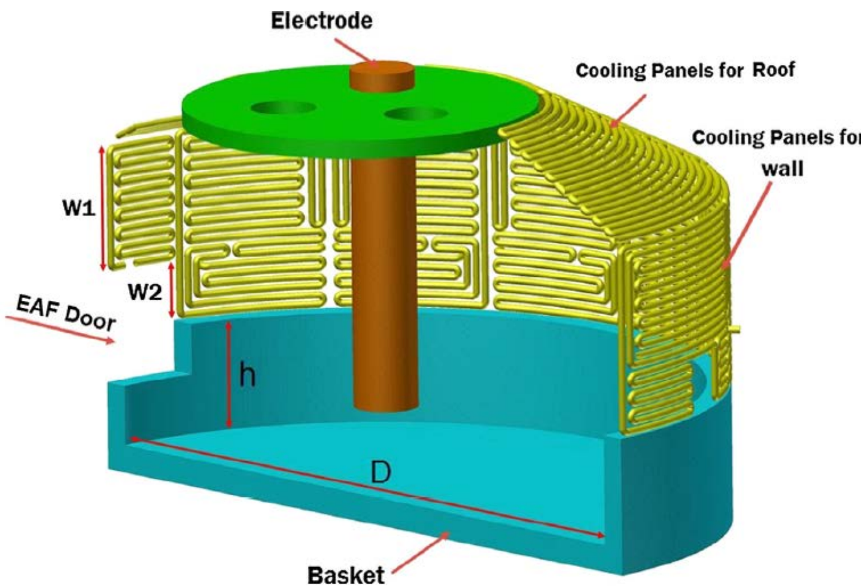

Figure 2.9 Schematic representation of the EAF geometry [20].

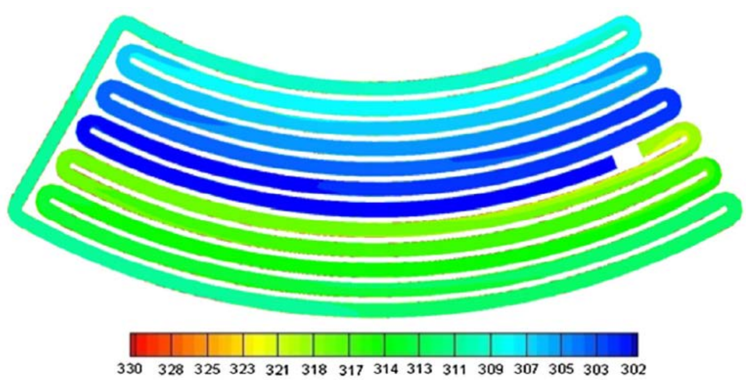

Figure 2.10 Temperature contour of water panel at cap joint [20].

In 2018, Mombeni et al. developed and studied a transient case of heat transfer in the WCP on the roof of an EAF during the charging process [21], which is shown in Figure 2.11. In this study, a process of roof rotation during charging was simulated. The roof was rotated to open the furnace, exposed to the ambient air, then the roof would be rotated back to close the furnace and exposed to the hot gas inside the furnace. Figure 2.12 shows such a fluctuation of temperature during the whole process. Such a temperature variation could be repeated by 15 times a day, and such a thermal fatigue would damage the water-cooling panel. In the meantime, this study also gave a prediction of temperature distribution of water inside the panels, as shown in the Figure 2.13. It could be seen that the temperature near the bend would be higher, because the water stream may be slowed down to carry less heat. At the end of this paper, a water-cooling panel in circular shape was suggested to reduce the risk of overheating.

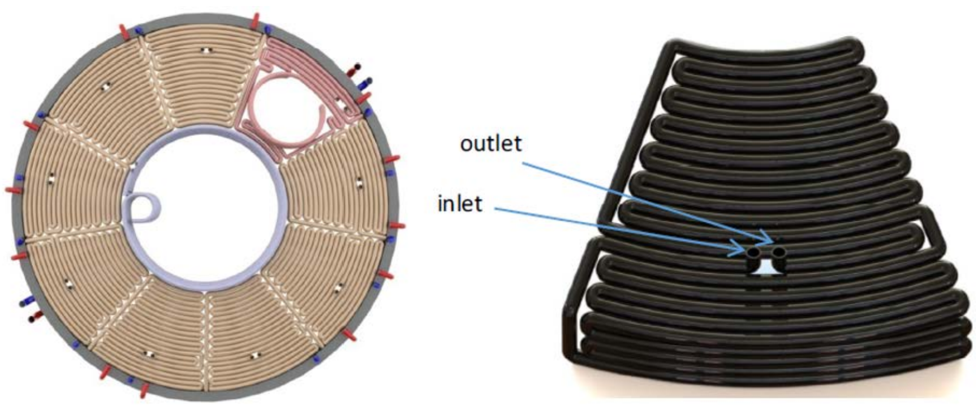

Figure 2.11 Top view of complete roof and a single water-cooling panel [21].

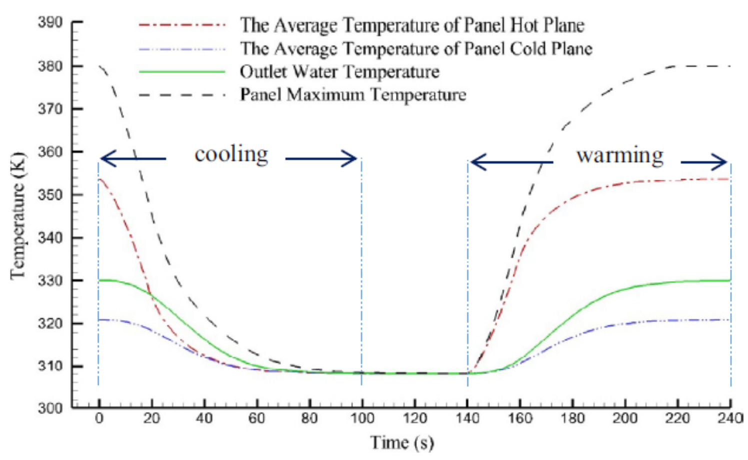

Figure 2.12 Panel temperature changes during cooling and warming stages [21].

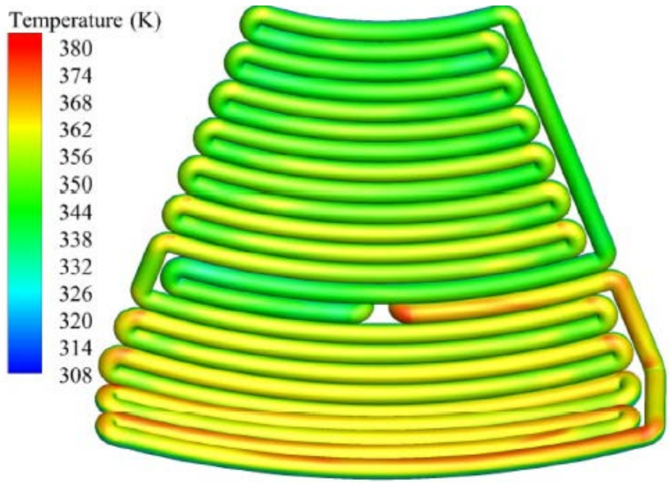

Figure 2.13 Temperature distribution in the warm side of the panel [21].

Some researchers were focused on the heat transfer in a larger scale, considering the heat from electric arc to the overall side wall or the roof. In 2012, Sanchez et al. studied the influence of slag height to hot spots [22]. As shown in Figure 2.14, Sanchez et al. developed a CFD AC EAF model to simulate the temperature distribution on the furnace walls. Channel arc model (CAM) was utilized to calculate the parameters of the arc in this paper. Discrete ordinates (DO) model was used to simulate the radiation power from electric arcs, 25% of total arc power was determined to be released in form of radiation heat.

Figure 2.15 shows simulated temperature distribution in this paper with a function of slag height. It can be seen that with increased slag height, less electrode arc will be exposed and less radiation heat will be transmitted to the side wall, hence cause the fewer hot spots and lower temperature.

In Mandal et al.'s paper, chemical reactions were not considered, meaning that the gas inside the furnace was all air and no injection of jets was considered in this paper.

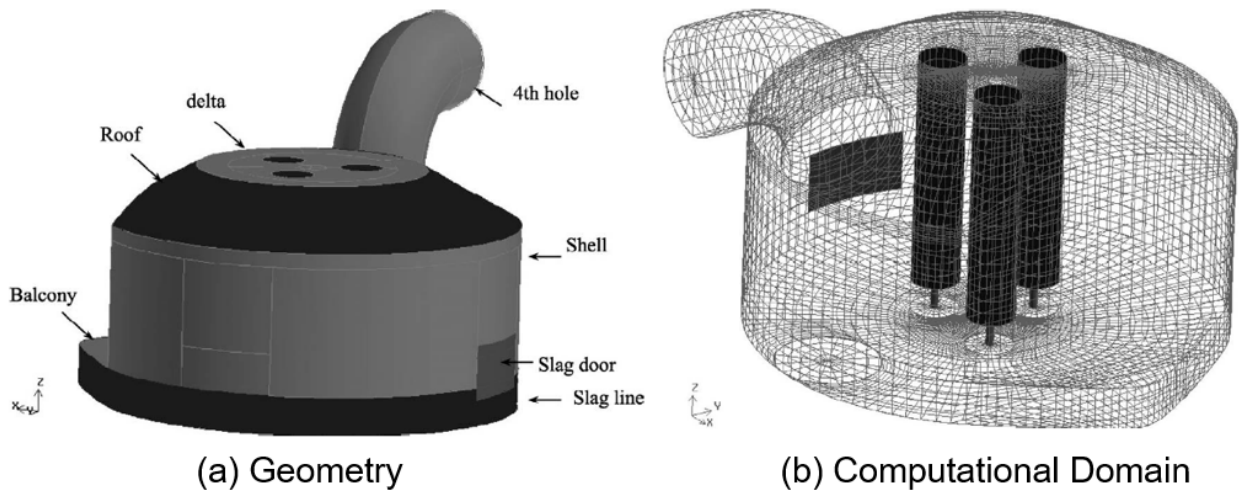

Figure 2.14 Geometry (a) and computational domain (b) in Mandal et al.'s paper [22].

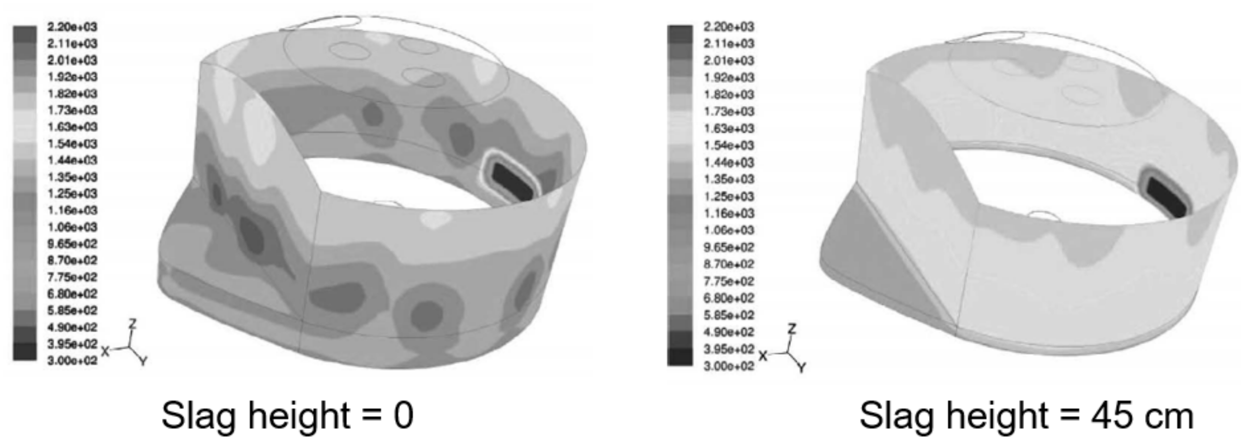

Figure 2.15 Temperature distribution with a function of slag height [22].

In 2016, Gruber et al. [23] developed a numerical model to investigate the influence of arc region on heat and mass transfer in freeboard. As shown in Figure 2.16, a free burning arc was generated below the electrode, an electron flow with high velocity and high temperature was blown down to the bottom and furtherly heated the gas of the domain. A simulated temperature contour is shown in Figure 2.17, it can be noticed that the free burning arc can influence the hot spots distribution on side wall. In this paper, a CO source was considered at the bottom slag layer, and air leakage from different gaps was considered, so that the flow field of the furnace could be simulated, as shown in Figure 2.18, from bottom to the top exhaust.

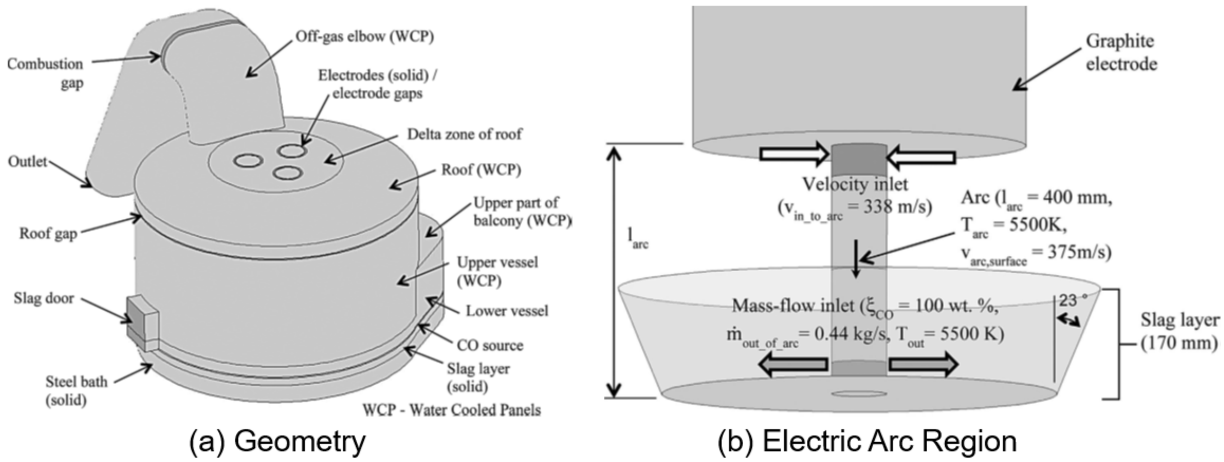

Figure 2.16 Geometry (a) and electric arc region (b) in Gruber et al.'s paper [23].

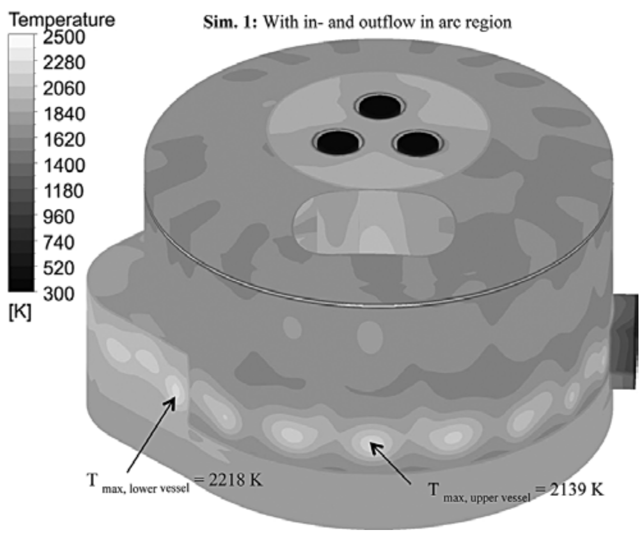

Figure 2.17 Temperature distribution on the EAF walls [23].

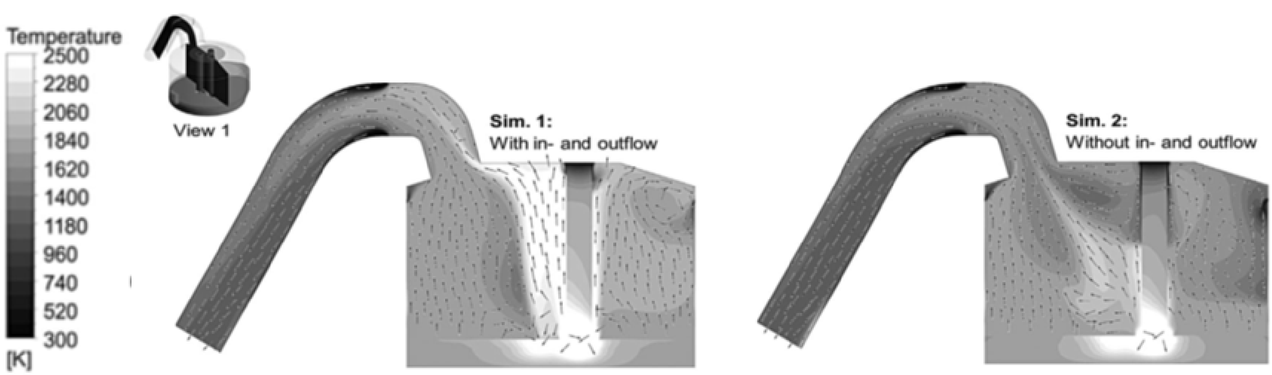

Figure 2.18 Influence of the arc region on the simulated temperature distribution [23].

In 2016, Yigit et al developed a CFD model to consider both electrode radiation and carbon injection inside the furnace, as shown in Figure 2.19 [24]. Their research simulated the temperature distribution on the bottom surface in Figure 2.20. Their research also proved that radiation power inside the furnace is dominant as shown in Figure 2.21.

The limitation of this research is that only carbon injection was considered, rather than complete fuel and oxygen jet, meaning that the energy input may be not accurate. In the meantime, the energy input from arc was released from the electrode tip rather than arc column, this may also influence the accuracy.

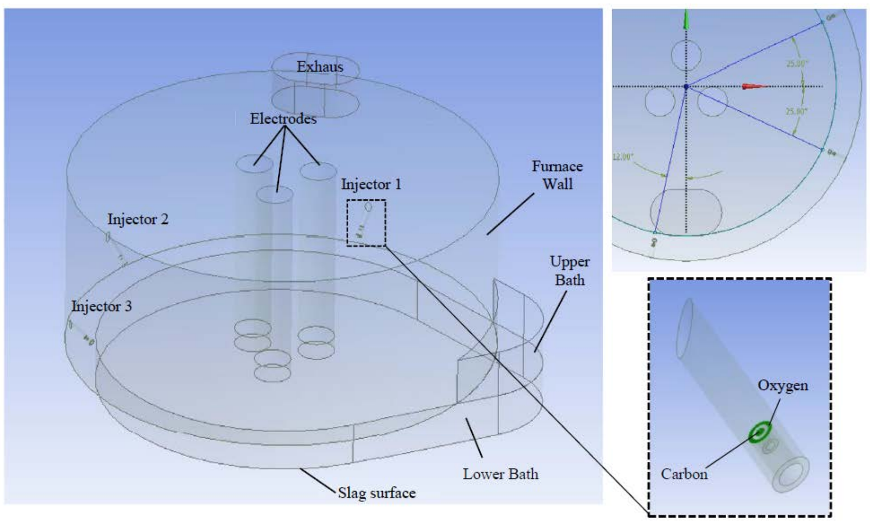

Figure 2.19 Geometry in Yigit's paper [24].

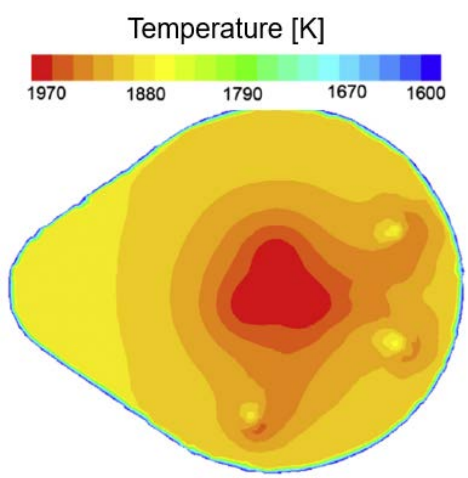

Figure 2.20 Temperature distribution on the slag surface [24].

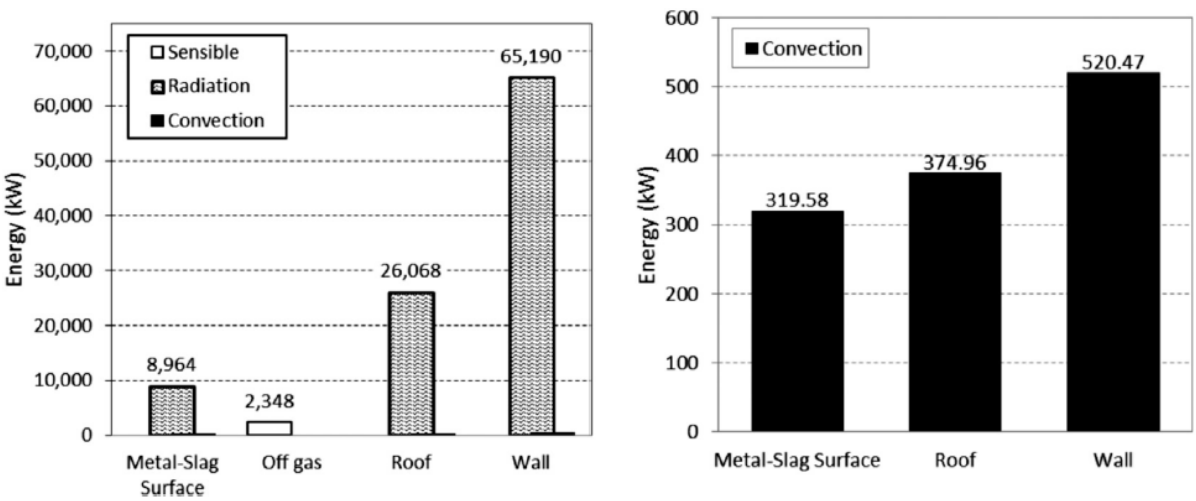

Figure 2.21 Heat output in radiation, convection and off-gas [24].

3. NUMERICAL MODELS

A freeboard simulator is utilized to simulate the condition of the freeboard. The model considers the combustion of fuel and oxygen, and the heat flux of central electric arc. The modeling in this article has following assumptions:

1) The model is a steady case, simulating a moment during the refining stage.
2) The post combustion is assumed uniformly on the slag surface, so that the CO generation is uniformly distributed on the bottom slag surface.
3) The burner condition is in lance mode, so that central oxygen jet is supersonic.
4) The gas flow is compressible ideal gas.

In order to simulate the phenomena in freeboard during refining stage, the simulator is composed by several numerical models: coherent jet model to calculate the flow field of gas phase, DC electric arc model to calculate the conditions of the central DC arc, slag foaming model to calculate the slag foaming status, which will determine the boundary of simulation domain.

3.1 Coherent Jet Model

The coherent jet model used in this project is based on a coherent jet model developed by researchers before [9][10][11]. This model is composed by a series of governing equations and models to simulate the flow field with a consideration of coherent jet injection and freeboard post-combustion. Compared to the previous model, the coherent model used in this project is simplified to reduce the computation resource, for the reason that the liquid bath is not considered in this project, and coherent jet penetration ability is not that important.

3.1.1 Governing Equations

A series of governing equations including continuity, momentum, turbulence and energy are written in Cartesian coordinate system for the steady-state condition in gas phase [10].

Equation of continuity

$$\nabla(\rho\vec{v}) = 0 \tag{17}$$

Equation of momentum

$$\nabla(\rho\vec{v}\vec{v}) = -\nabla p + \nabla(\bar{\bar{\tau}}) + \rho\vec{g} + \vec{F} \tag{18}$$

Equation of energy

$$\frac{\partial}{\partial x_i}[u_i(\rho E + \rho)] = \frac{\partial}{\partial x_j}\left[k_{eff}\frac{\partial T}{\partial x_i} - \sum_j h_j\vec{J}_j + \left(\bar{\bar{\tau}}_{eff}\cdot\vec{v}\right)\right] + S_h \tag{19}$$

$$k_{eff} = k + \frac{c_p\mu_t}{Pr_t} \tag{20}$$

Where ρ, $\bar{\bar{\tau}}$, $\rho\vec{g}$, and $\vec{F}$ are the density, stress tensor, gravitational body force and external body force. k_{eff} , $\vec{J}_j$, and Pr_t are the effective thermal conductivity and diffusion flux of species j and turbulent Prandtl number. The turbulent Prandtl number here is 0.85. S_h, E, h , and c_p are the heat of chemical reaction, total energy, sensible enthalpy and specific heat, respectively.

3.1.2 Turbulence Model

The standard k-epsilon model is used in the original coherent jet model.

Equation of turbulent kinetic energy, k

$$\frac{\partial}{\partial x_i}(\rho k u_i) = \frac{\partial}{\partial x_j}\left[\left(\mu + \frac{\mu_t}{\sigma_k}\right)\frac{\partial k}{\partial x_j}\right] - \rho\overline{u_i}\overline{u_j}\frac{\partial u_j}{\partial x_i} - \rho\varepsilon - \rho\varepsilon {M_\tau}^2 \tag{21}$$

Equation of turbulence dissipation rate, ε

$$\frac{\partial}{\partial x_i}(\rho\varepsilon u_i) = \frac{\partial}{\partial x_j}\left[\left(\mu + \frac{\mu_t}{\sigma_\varepsilon}\right)\frac{\partial k}{\partial x_j}\right] - C_{\varepsilon 1}\rho\overline{u_i}\overline{u_j}\frac{\varepsilon}{k}\frac{\partial u_j}{\partial x_i} - \rho C_{\varepsilon 2}\frac{k^2}{\varepsilon} \tag{22}$$

Where μ and μ_t are the molecular viscosity and the turbulent viscosity. M_τ is the turbulent Mach number defined as the following equation. σ_k, σ_ε, are the turbulent Prandtl number for k with a value of 1.0, and turbulent Prandtl number for ε with a value of 1.3. $C_{\varepsilon 1}$ and $C_{\varepsilon 2}$ are constants with values of 1.44 and 1.92.

$$M_\tau = \frac{\sqrt{2k}}{a} \tag{23}$$

Where $a = \sqrt{\gamma RT}$ is the acoustic velocity (m/s).

The turbulent viscosity μ_t is defined as below:

$$\mu_t = C_\mu \rho\frac{k^2}{\varepsilon} \tag{24}$$

Where C_μ is 0.09 in the standard k-epsilon turbulence model. In this paper, the C_μ is modified as:

$$C_\mu = \frac{0.09}{C_T} \tag{25}$$

$$C_T = 1 + \frac{1.2{T_g}^{0.6}}{1 + f(M_\tau)} \tag{26}$$

Where T_g is the normalized local total temperature gradient, which is a function of k and ε:

$$T_g = \frac{|\nabla T_t|(k^{\frac{3}{2}}/\varepsilon)}{T_t} \tag{27}$$

Where T_t is the local total temperature (K). The function $f(M_\tau)$ related to the turbulent Mach number is considered:

$$f(M_\tau) = ({M_\tau}^2 - {M_{\tau 0}}^2)H(M_\tau - M_{\tau 0}) \tag{28}$$

$H(x)$ is the Heaviside function, and $M_{\tau 0}$ is 0.1. A user-defined function (UDF) code was developed by the researchers to realize the correction on C_μ [10].

3.1.3 Simplified Turbulence Model

In this project, since only the part of the jet in freeboard is considered, and the penetration ability is not important, the turbulence model is simplified by utilizing the shear-stress transport (SST) $k - \omega$ turbulent model and no consideration of the correction on C_μ.

Equation of turbulent kinetic energy, k

$$\frac{\partial}{\partial x_i}(\rho k u_i) = \frac{\partial}{\partial x_j}\left(\Gamma_k \frac{\partial k}{\partial x_j}\right) + G_k - Y_k \tag{29}$$

Equation of specific dissipation rate, ω

$$\frac{\partial}{\partial x_j}(\rho \omega u_j) = \frac{\partial}{\partial x_j}\left(\Gamma_\omega \frac{\partial \omega}{\partial x_j}\right) + G_\omega - Y_\omega + D_\omega \tag{30}$$

Where G_k, G_ω, Γ_k, Γ_ω, Y_k, Y_ω, D_ω, are the production of k, generation of ω, effective diffusivity of k, effective diffusivity of ω, dissipation of k due to turbulence, dissipation of ω due to turbulence, and the cross-diffusion term, respectively.

3.1.4 P1 Radiation Model

P1 model was selected to solve the radiation heat transfer inside the furnace. As a basic radiation model, P1 model has been widely used in numerical simulation. Scheepers has proved that P1 model is effective to solve the problems in EAF in 2010 [25]. P1 model treats the expansion of the radiation intensity I into an orthogonal series of spherical harmonics [26]. The P1 equation can be illustrated as:

$$\nabla(q_r) = \nabla T\left(k_{eff}\nabla T\right) \tag{31}$$

Where q_r is the radiation flux in $W \cdot m^{-2}$.

3.1.5 Species Transport Model

In the gas phase, both supersonic coherent jets and post combustion have been considered, the reaction of the components can be simulated by species transport model. A volumetric reaction is considered to enable the combustion within methane and oxygen, since methane, or CH_4 is used for the fuel of burners. A series of species conservation equation has been applied in this model:

$$\begin{aligned}\frac{\partial}{\partial t}(\rho Y_i) + \frac{\partial}{\partial x}(\rho u Y_i) + \frac{\partial}{\partial y}(\rho v Y_i) + \frac{\partial}{\partial z}(\rho w Y_i) \\ = -\frac{\partial}{\partial x}(\vec{J_i}) - \frac{\partial}{\partial y}(\vec{J_i}) - \frac{\partial}{\partial z}(\vec{J_i}) + R_i\end{aligned} \tag{32}$$

Where Y_i, $\vec{J_i}$, and R_i are the mass fraction of species i, the diffusion flux term of species i, and the net rate of production of species i by chemical reaction. $\vec{J_i}$ arises due to gradients of concentration and temperature, under which the diffusion flux can be written as:

$$\begin{aligned}\vec{J_i} = -\left(\rho D_{i,m} + \frac{\mu_t}{Sc_t}\right)\left(\frac{\partial}{\partial x}(Y_i) + \frac{\partial}{\partial y}(Y_i) + \frac{\partial}{\partial z}(Y_i)\right) - \frac{D_{T,i}}{T}\ (\frac{\partial}{\partial x}(T) + \frac{\partial}{\partial y}(T) \\ + \frac{\partial}{\partial z}(T)\end{aligned} \tag{33}$$

Where $D_{i,m}$, Sc_t, and $D_{T,i}$ are the diffusivity for species i with the value of $2.88*10^{-5}$ m^2/s, the turbulent Schmidt number, which is 0.7, and the thermal diffusion coefficient.

In the original coherent jet model, a 28-step reaction of methane and air was considered [10]. To reduce computational time, in this paper, a 2-step reaction of methane combustion is considered. The gas inside the furnace is treated as a mixture including methane, oxygen, carbon monoxide, water, carbon dioxide and nitrogen. The properties of the mixture gas follow mixing-law, determined by the properties of species. The parameters of 2-step reaction have been presented in Table 3.1. Since the post combustion is mainly composed by the CO released from bottom slag layer, such a phenomenon can be covered in the methane-air 2-step reaction.

Table 3.1. Reaction mechanism.

No.	Reactions	Rate equations	A	b	E
1	$CH_4 + 1.5O_2 \rightarrow CO + 2H_2O$	$\frac{d[CH_4]}{dt} = AT^b e^{-E/RT} \cdot [CH_4]^{0.7}[O_2]^{0.8}$	5.012×10^{11}	0	2.0×10^8
2	$CO + 0.5O_2 \rightarrow CO_2$	$\frac{d[CO]}{dt} = AT^b e^{-E/RT} \cdot [CO]\,[O_2]^{0.25}$	2.239×10^{12}	0	1.7×10^8

3.2 DC Electric Arc Model

The DC electric arc model is developed to calculate arc power and arc length about the DC electric arc based on the provided voltage and current.

3.2.1 DC Electric Arc Power

To obtain the parameters used for simulation, the Channel Arc Model (CAM) is utilized. At present, CAM is proper to compute the arc temperature, arc radius and instantaneous power [22]. Compared to AC arc, voltage and current are constant in a DC arc. CAM assumes that arc is in the shape of cylinder. Arc power is conducted into the furnace in different ways: convection, radiation, and gas heating and electrode loss. Convection and radiation make up the most proportion in the arc power. Previous researchers have studied different shares of arc heat dissipation [8]. In mathematical modeling of Alexis et al in 2000, share of arc heat dissipation by radiation is 45% [27]. In CFD simulation by Guo and Irons in 2003 and system modeling by MacRosty and Swartz in 2005, shares of radiation are both 80% [28] [29]. In a literature review of Bowman and Kruger in 2009, radiation composes 39% [30]. For a system modeling by Logar et al. in 2012, radiation makes up 75% of total arc heat dissipation [31]. According to these papers, the heat delivered to freeboard by radiation is 75% of total arc power in this paper. Radiation arc power, P_r, can be calculated in the following equation:

$$P_r = 75\% \cdot UI \tag{34}$$

For a sample electrode operating condition with U = 795.8 V, and I = 133.8 kA, total input arc power is 106.5 MW, so that 75% of the total arc power, or 79.875 MW of the power will be delivered to the freeboard.

3.2.2 DC Electric Arc Length

DC electric arc length model is to calculate the total arc length. Jones [12] summarized the results of a series of experimental work to obtain an equation to calculate the voltage from current and arc length of DC arc. The calculation of voltage is shown in equation (9).

Based on Jones' work, a fitting equation to calculate the arc length from voltage and current. This fitting equation can be used for arc length in range of 10 cm ~ 110 cm and current in range of 20 kA ~ 180 kA. The calculation process has been shown in equation (35).

$$L_{A,t} = \boldsymbol{A} + \boldsymbol{B}U + \boldsymbol{C}I + \boldsymbol{D}U\text{^}2 + \boldsymbol{E}UI + \boldsymbol{F}I\text{^}2 \tag{35}$$

A = -7.845, B = 0.1257, C = -0.2831, D = 4.328e-05, E = -2.458e-04, F = 1.033e-03

$L_{A,t}$ is the total arc length in cm.

This equation an be used for a voltage range from 360 V to 1000 V. For electrode conditions of 795.8 V and 133.8 kA, the total arc length can be calculated out as 74.04 cm, or 29.15 inch.

3.3 Slag Foaming Model

To describe the slag foaming phenomenon numerically, slag foaming model is developed to calculate the foaming height. During the slag foaming phenomenon, compared to the foaming height, the initial height of slag layer is too little, hence the foaming height is used to describe the total height of slag layer. In the past years, many researchers have investigated the method to calculate the foaming height. In 1989, Ito and Fruehan [14] developed up an equation to calculate the foaming height H_f (m) from foaming index Σ (s) and superficial velocity v_g (m/s):

$$H_f = \Sigma \cdot v_g \tag{36}$$

Superficial velocity (v_g) of post combustion gas is obtained from the foaming rate of carbon monoxide. Based on the data provided, 1670.7 kg of the carbon was charged into the furnace. All of the carbon is assumed to generate CO, and the emission of CO is assumed linear during the period of 1200 s of refining stage. Therefore, the CO release rate is 3.287 kg/s, and value of the superficial velocity is calculated as 0.3167 m/s.

The foaming index (Σ) is a parameter to describe the average travelling time of the gas in the generated foam. This parameter is calculated from properties of slag. In 1991, Jiang and Fruehan [16] presented an expression to calculate the foaming index based on slag properties:

$$\Sigma = 115 \frac{\mu_s}{\sqrt{\sigma_s \rho_s}} \tag{37}$$

where μ_s, σ_s, and ρ_s are slag viscosity, slag surface tension and slag density, respectively.

These slag properties are influenced by slag composition. The basic components of EAF slag are: CaO, FeO, Al_2O_3, SiO_2, MgO and MnO. Surface tension has been obtained from the experiment results of Wu et al. [32] and Xuan et al. [33]. The surface tensions and densities of the slag components are in a function of temperature and they have been presented in Table 3.2.

For viscosity, researchers have found that viscosity of the slag have significant influence on foaming effect. Pretorius described the relationship of foaming index with viscosity schematically [34]. As shown in Figure 3.1, increasing slag viscosity, which is mainly determined by the input of basic components like CaO and MgO, usually represents the accumulation of solid particles. When solid particles are firstly accumulated, gas bubbles of slag layer will be easier to be sustained. Thus, the slag foaming has been increased. However, with further viscosity increase, if the slag is oversaturated by CaO or MgO, too many solid particles will reduce the slag foaming reversely. In this study, the calculation of foaming index is considered in only the section before over-saturation of the slag. Therefore, current model is unable to predict an optimal slag. In 2011, Kenneth Mills summarized a series of models to calculate out the slag viscosity [35] - [40]. Among these papers, Urbain in 1987 provided a model to calculate the viscosity for a wide range of scrap [37]. In this study, Urbain's model is utilized to calculate the viscosity. An equation in form of Weymann relation is utilized to calculate the viscosity.

$$\mu_s(dPa \cdot s) = A \cdot T \cdot exp(1000B/T) \tag{38}$$

Where T is temperature in K, A, B have a relation as:

$$-lnA = 0.2693\, B + 11.6725 \tag{39}$$

To obtain B, slag mole fractions would be required. In this paper, slag constituents were divided into 3 types:

Glass formers: $X_G = X_{SiO2}$

Network modifiers: $X_M = X_{CaO} + X_{MgO} + X_{FeO} + X_{MnO}$

Amphoterics: $X_A = X_{Al2O3}$

For a species i, X_i represents the mole fraction of this certain species. Based on the mole fractions, a parameter α is induced to help calculate the value of B:

$$\alpha = X_M/(X_M + X_A) \tag{40}$$

$$B_i = a_i + b_i\alpha + c_i\alpha^2 \tag{41}$$

With the parameters B_i, B can be calculated with X_{SiO2}:

$$B = B_0 + B_1X_{SiO2} + B_2X_{SiO2}^2 + B_3X_{SiO2}^3 \tag{42}$$

The values for a_i, b_i, and c_i for each species of CaO, MgO and MnO has been listed in Table 4.2, with the value of each species, a mean value of B can be calculated out:

$$B_{global} = (X_{MnO}B_{MnO} + X_{CaO}B_{CaO} + X_{MgO}B_{MgO})/(X_{CaO} + X_{MgO} + X_{MnO}) \tag{43}$$

The mean value, B_{global}, can be used to calculate out the final viscosity.

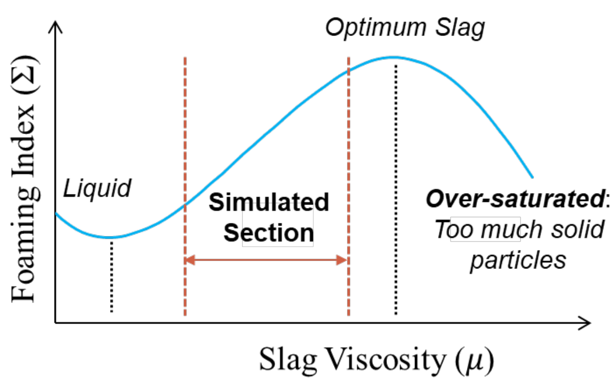

Figure 3.1. Relationship of foaming index and slag viscosity.

Table 3.2. Temperature dependency of slag surface tension and density.

Species	Surface Tension σ_s (mN/m)	Density ρ_s (kg/m^3)
CaO	791 – 0.094 T (K)	3240 – 0.2 T (K)
FeO	504 + 0.098 T (K)	1950 + 1.86 T (°C)
Al_2O_3	1020 – 0.177 T (K)	3040 – 1.15 (T - 2303) (K)
SiO_2	243 + 0.031 T (K)	2510 – 0.213 T (°C)
MgO	1770 – 0.636 T (K)	3600
MnO	988 – 0.179 T (K)	5400

Table 3.3 Numerical values of the coefficients in Equation (32) for the three oxides [37].

i	a_i all	b_i Mg	Ca	Mn	c_i Mg	Ca	Mn
0	13.2	15.9	41.5	20.0	-18.6	-45	-25.6
1	30.5	-54.1	-117.2	26	-104.6	130	-56
2	-40.4	138	232.1	-110.3	-112	-298.6	186.2
3	60.8	-99.8	-156.4	64.3	97.6	213.6	-104.6

Table 3.4. Sample slag composition.

Species	CaO	FeO	Al_2O_3	SiO_2	MgO	MnO
Weight pct	25.53	41.4	4.78	11.53	7.15	4.87

Table 3.4 shows the composition of a sample slag from an industrial process in which water-cooling panel overheating issue appeared. Based on the equations (36) – (43), the foaming height of this slag sample can be calculated out as 30.66 cm, or 12.08 inch at 1473K, the temperature of freeboard.

In order to define the energy input of the electric arc and the influence of slag foaming phenomenon, 3 models have been developed to calculate out these parameters. The first model should be able to calculate the arc power. The second model and the third model are for the calculation of arc exposure.

3.4 Model Integration

Based on the DC electric arc model and slag foaming model, arc exposure can be calculated as:

$$L_{A,e} = L_{A,t} - H_f \tag{44}$$

Where $L_{A,e}$, $L_{A,t}$ and H_f are the exposed arc length, total arc length and foaming height. The relationship of these parameters is shown in Figure 3.2.

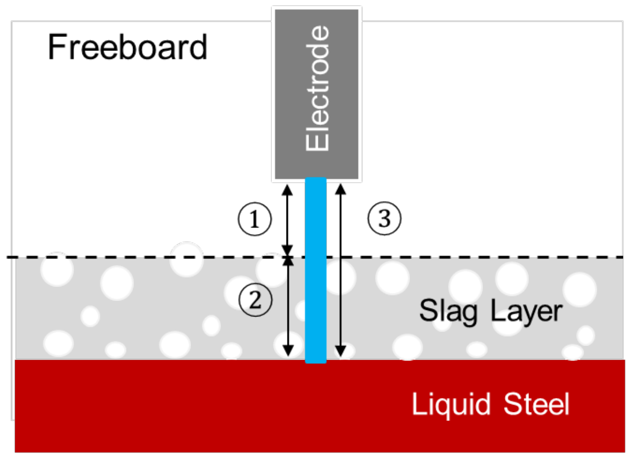

①: Exposed Arc Length $L_{A,e}$ ②: Foaming Height H_f

③: Total Arc Length $L_{A,t}$

Figure 3.2. Slag foaming parameters.

With the integration of the models, the calculated results can be input into the CFD freeboard simulator by determining the parameters of the simulation domain.

For the sample case with U = 795.8 V, and I = 133.8 kA and slag composition in Table 3.4, it can be calculated that total arc length is 29.15 inch, foaming height is 12.08 inch, and the exposed arc length will be 17.07 inch, which can be input into the CFD simulator.

4. COMPUTATIONAL DOMAIN AND BOUNDARY CONDITIONS

4.1 Computational Domain

The simulation domain is generated based on SSAB's arc furnace. It was a DC arc furnace, containing 160 ton of steel. As shown in the Figure 4.1, this geometry considers the EAF part above slag layer: freeboard, 1 DC electrode in the center, 5 burners around the side wall, and 1 exhaust outlet on the top. Each burner is composed by 3 types of injectors: single primary oxygen injector in the center, 12 fuel injectors and 12 secondary oxygen injectors at the outside.

The mesh is generated based on the EAF freeboard geometry as shown in Figure 4.2. The regular part of the freeboard is meshed in structural cell as much as possible to reduce the number of cells so as to save simulation time. Rest of the part is meshed by unstructured cells. The mesh is developed by ANSYS Meshing 19.1, and total mesh number is 4.80 million.

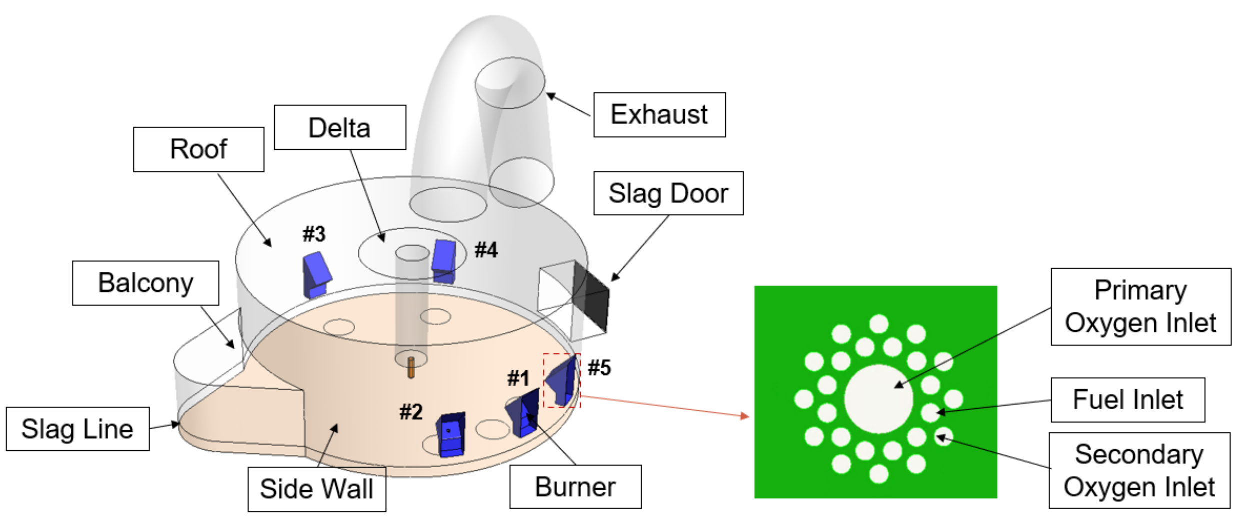

Figure 4.1. Geometry of the freeboard and burner.

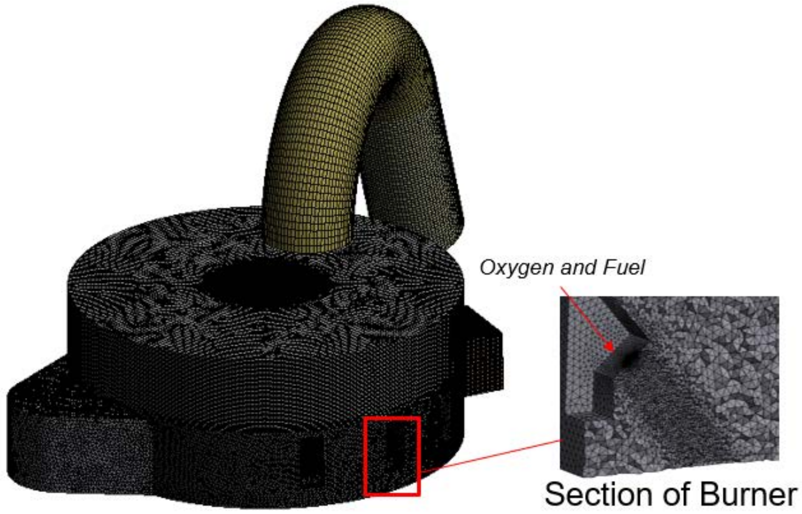

Figure 4.2 Mesh of the freeboard and section of burner.

4.2 Boundary Conditions

Boundary conditions of the CFD models are obtained from an EAF process charged with 175.8 tons of scrap.

The shell, top of balcony, roof, burner walls, side wall of the slag door and upper wall of exhaust are covered by WCP. The slag door is treated as closed and covered by WCP. The else walls, including the slag line, balcony side, burner wall, delta and lower part of exhaust are not covered by WCP, so the heat flux of these walls are treated as same to refractories. The slag door is closed so that the bottom surface and the slag door itself are treated as refractory wall. The values of material properties used by WCP and refractories are listed in Table 4.3.

For water cooling panels, according to the industrial data, sensors are set at the inlet of 1 panel and the outlets in 16 panels. The measured inlet temperature is 28.83 °C and the average of measured outlet temperature is 39.56 °C. Water flow rate is 190 kg/s. The absorbed heat flux is attributed uniformly on the side wall, the WCP heat flux can be computed out as −130.31 kW/m^2, the negative value means that the water-cooling panel is absorbing heat from the domain.

For refractories, the heat flux is -8.93 kW/m^2, according to Sanchez's paper [21]. The properties of refractories have been listed in Table 4.4.

Table 4.1. Material thermal properties.

Boundary	Material Type	Specific Heat, Cp (J/kg·K)	Thermal Conductivity, k (W/m·K)	Emissivity, ε
Water Cooling Panel	Steel	502	75.83	0.80
Refractory	MgO	874	4	0.31
Electrode	Graphite	710	230	0.85

Table 4.2. Wall properties.

Heat flux of WCP, kW/m^2	-130.31
Heat flux of refractory, kW/m^2	-8.93
Thickness of WCP, m	0.0254
Thickness of refractory, m	0.457

As shown in Figure 4.1, 5 burners on the side wall are installed to inject fuel or oxygen jets continuously. The burners are in burner mode to inject subsonic jets. The burner conditions are shown in Table 4.5. The amount of oxygen can react with fuel completely, making sure that the heat from burners is constant. The combusted hot gas can release heat into the furnace. The five regions located at the bottom surface represent the upper section of the cavity form by the jets on the bath. These surfaces are treated as outlets. The jets will leave the furnace through these 5 outlets.

Table 4.3. Burner Operating Condition

	#1	#2	#3	#4	#5
Central oxygen mass flow rate	0.857 kg/s (1154 SCFM)			0	
Fuel mass flow rate	0.0534 kg/s (70 SCFM)			0.0834 kg/s (520 SCFM)	
Shroud mass flow rate	0.0231 kg/s (68 SCFM)			0.389 kg/s (250 SCFM)	
Temperature of gas	300 K				

The bottom of the freeboard is the top surface of slag layer. In refining stage, reactions of oxides in slag and carbon generate post-combustion CO gas. In this paper, CO emission from the slag is distributed uniformly on the whole slag surface, and the mass flow rate of CO is 3.287 kg/s. The temperature of post-combustion gas is 1473 K, which is the temperature of freeboard [39]. The distribution of the boundaries is shown in the Figure 4.3.

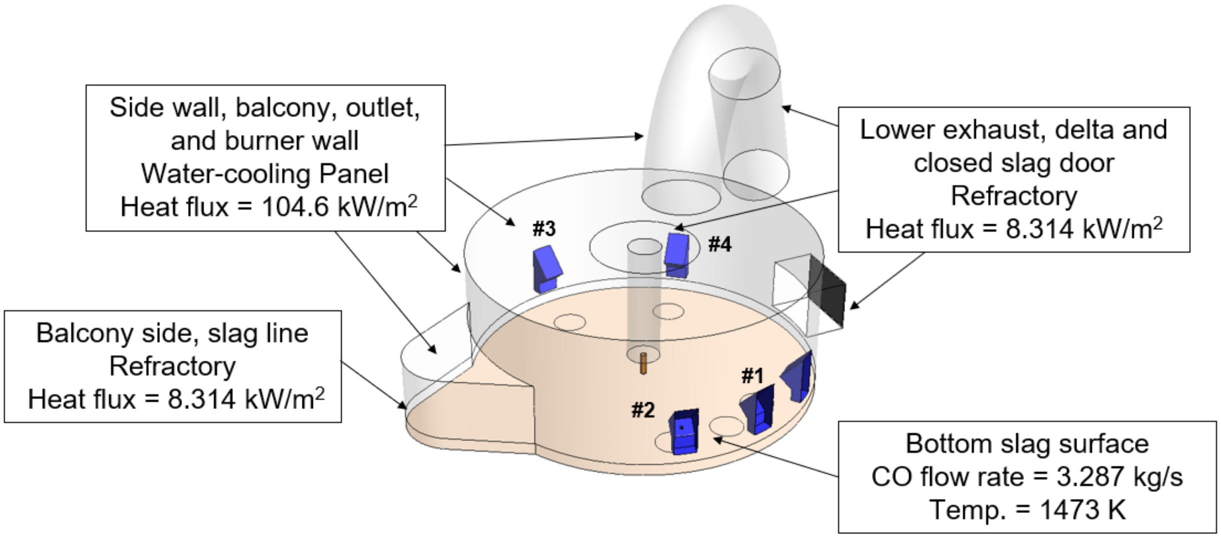

Figure 4.3. Boundary conditions.

For electrode, temperature on the surface of the electrode is treated as a function of distance from the tip of electrode according to Sanchez's paper [22]. The bottom of the tip is treated as 3700 K, and it will be decreased gradually to 700 K at the top of the electrode. The temperature plot has been shown in Figure 4.4.

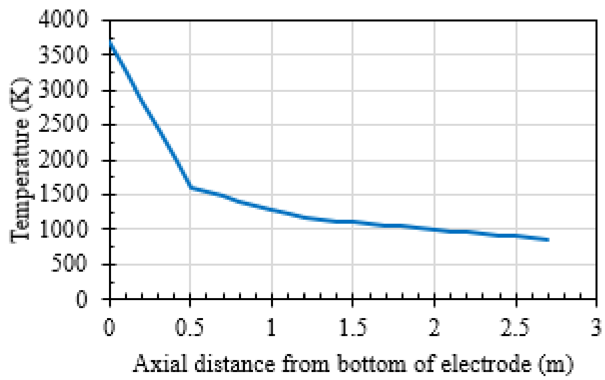

Figure 4.4. Temperature plot with a function of distance from bottom of electrode.

The boundary of arc column is related to arc operating conditions. In steelmaking process, electric arc will be covered by slag layer so that the covered part of arc will heat up the slag, and the uncovered part will release the radiation heat to freeboard directly. In this paper, the power delivered to electrode and slag is treated as a fixed temperature on each boundary. The arc model is utilized to calculate the radiation power delivered to freeboard.

The distance from the electrode tip to the slag layer is the total arc length. In this paper, total arc length is around 25 inch, or 63.5 cm based on industrial data. The actual arc length will be determined by the location of electrode tip and slag level. From CAM, the diameter of the cylinder is calculated out as 4.5 inch, or 11.43 cm. The radiation power is distributed uniformly on the side face of the cylinder, and the heat flux is 3.454e+7 W/m^2. For the conditions that the arc is totally covered, the exposed arc column heat flux will be 0.

Since arc plasma will influence the flow field significantly by accelerating it, like mentioned in Gruber's paper [23]. In this paper, the arc plasma is considered by adding a fixed velocity of 1000 m/s in vertical direction to simulate a more proper flow field.

5. SIMULATION RESULTS AND DISCUSSION

5.1 Validation

In this project, industrial data from SSAB is used to validate the freeboard simulator. From the heat where overheating alarm was triggered, it is found that when arc power is kept at 72.5 MW, water panel overheating issue did not appear, but if arc power is above 99.1 MW, overheating issue took place. Average voltage and current for the power of 72.5 MW are 589.0 V and 123.1 kA, respectively, these parameters for the period of 99.1 MW are 718.3 V and 137.9 kA. Accordingly, the exposed arc length can be calculated out as 5.33 inch and 11.96 inch, and CFD simulation results have been shown in Figure 5.1 and Figure 5.2.

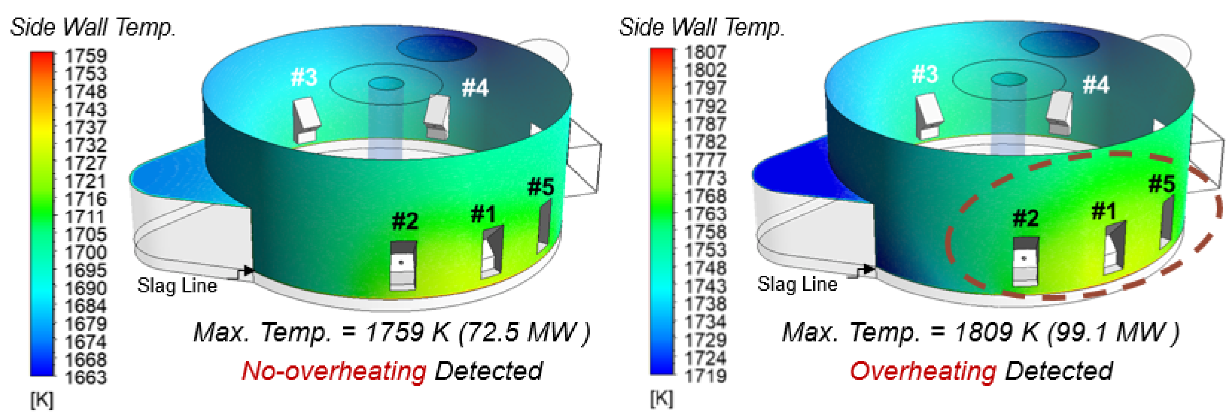

Figure 5.1. Side wall temperature distribution of cases with a function of arc power.

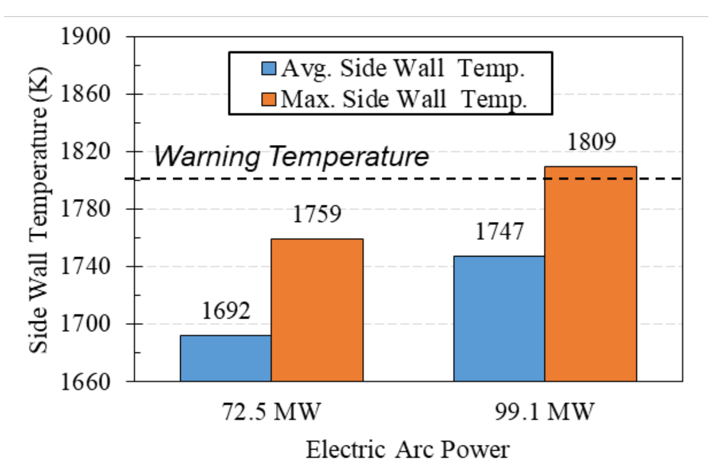

Figure 5.2. Temperature bar chart of cases with a function of arc power.

From Figure 5.1, it can be seen that the high temperature area is focused on the side with 3 burners, it is because that the side with 3 burners injecting more energy. In the meanwhile, the side with 2 burners is near to the exhaust so that hot gas can be easier to be released through the exhaust. The highest temperature appears at the junction of side wall with slag line, because the heat absorbed by slag line is much less than that of the WCP covered side wall.

According to Sanchez's paper [21], 1800 K is used to judge whether the overheating issue appears. From Figure 5.2, it can be seen that when arc power is set as 72.5 MW, the maximum wall temperature is 1759K, below the warning temperature. For the case with 99.1 MW arc power, the maximum temperature will be increased to 1809 K, higher than 1800 K, so that the overheating issue will take place in this case. As a conclusion, this simulator can be used to predict the overheating issue.

According to the information provided by SSAB, overheating issue was more likely to appear at the water panels near the slag door. One explanation to this phenomenon is that in this simulator, the slag door is totally closed but in real operation, there may be some air leakage through the gaps of slag door. The leaked air would react with the combusted gas, hence increase the wall temperature surrounded.

5.2 Analysis of Baseline Results

The comprehensive simulator has been coupled with a series of models to simulate the influence of electric arc, coherent jet and slag foaming. In this section, simulation results of the case with arc power of 72.5 MW will be analyzed, including flow field, species distribution and inside gas temperature.

For gas species distribution, in Figure 5.3 (a), it can be seen that CO released from bottom slag layer has been accumulated at the lower zone of the furnace especially the balcony part and slag door part. As the CO gas rises from the bottom, vortexes are generated at the upper zone of the furnace, this can explain why CO may be accumulated at the balcony and slag door, because these parts are away from burners or central arc column, the gas flow there is not strong to take the CO gas away. As shown in Figure 5.3 (b), CO_2 is less likely to be accumulated at the lower zone of the furnace. One reason is that these zones are fulfilled by CO gas, another reason is that CO_2 is mainly generated from combustion, by both methane from burners or CO from bottom slag layer. This will make CO_2 gas have higher temperature, and more likely to rise up. To investigate the variation of gas mass fraction in vertical direction, several section planes are selected with increased distance from the slag layer. The plot Figure 5.4 in shows area average gas mass fraction of CO and CO_2 on these section planes. It can be seen that as the plane being higher, CO mass fraction is decreased and reversely does CO_2 mass fraction. It is because that CO gas is mainly released from the bottom slag layer, as plane being farther from the slag layer, more CO gas will be combusted to CO_2. For a distance larger than 60 inches, there will be almost no CO gas combusted, so that both CO and CO_2 concentration will be kept at the same.

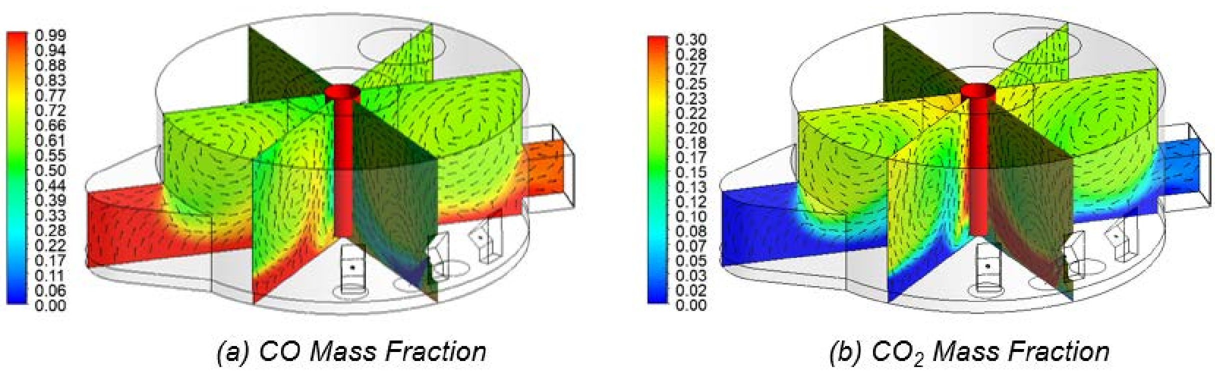

Figure 5.3 Contours of CO mass fraction and CO_2 mass fraction with velocity vectors.

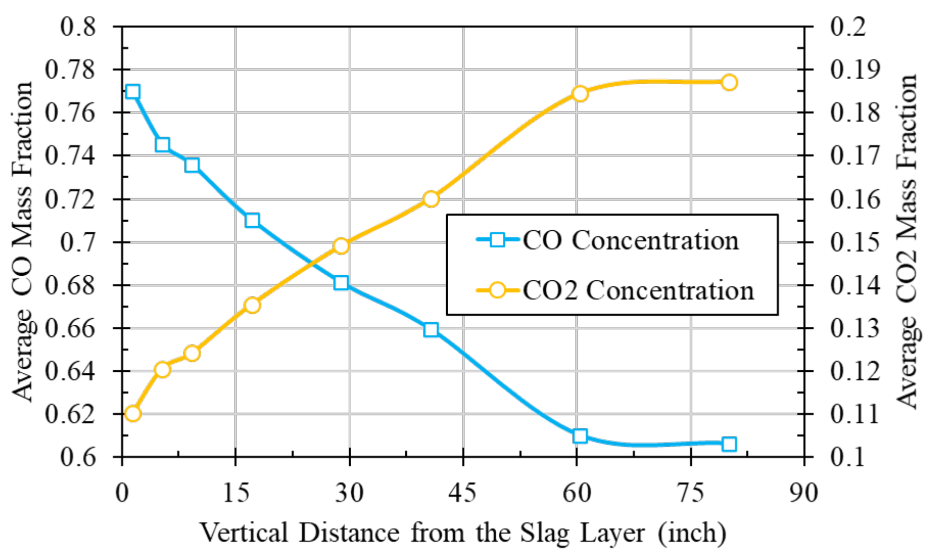

Figure 5.4 Average gas mass fraction plot with a function of vertical distance from the slag layer.

For temperature contour inside the furnace, as shown in Figure 5.5, the combusted gas from burners will rise up, get mixed with the hot gas near the electrode, then rise to the top of the furnace, and generate vortexes at the top. The high temperature gas with lower density tends more to be accumulated at the top of the furnace.

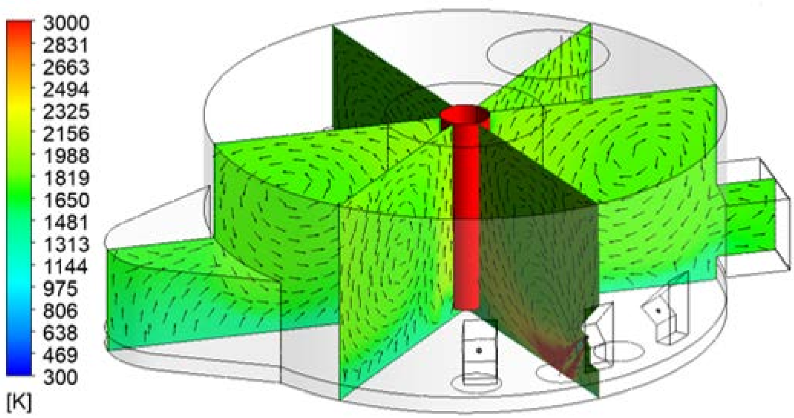

Figure 5.5 Temperature distribution inside the furnace.

For flow field inside the furnace, Figure 5.6 shows a streamline from gas inlets and top outlet. The hot gas vortexes can be found easily in this streamline figure. It can also be found that hot gas will tend to flow out through top outlet, this will increase the flowability of the gas. With more gas accumulated at the side with 3 burners, and more gas flowing out at the side with 2 burners, as well as more energy input through burners, it can be explained that hot spots may appear at the side with 3 burners.

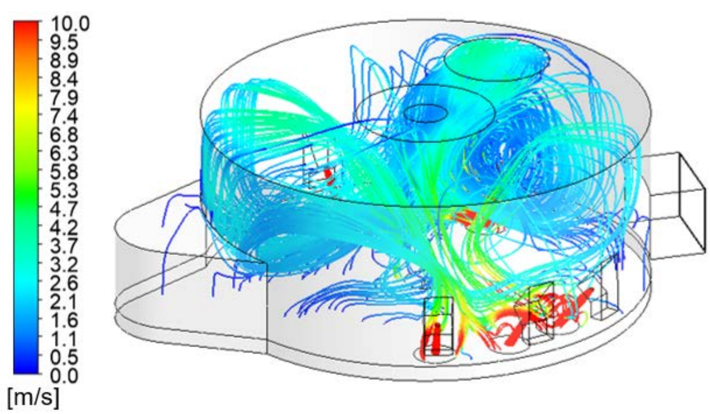

Figure 5.6 Streamline from burners and outlets colored by velocity.

5.3 Parametric Studies

This developed freeboard simulator can be applied to investigate the parameters that may influence the side wall temperature distribution. In the industrial steelmaking process, operating conditions are changeable, and effect of these operating conditions can be studied via CFD model. In this paper, a series of parametric studies was conducted. Parameters like arc power, slag level, burner condition, electric arc condition and cooling water flow rate were investigated in this paper.

5.3.1 Effect of arc power

A group of electric arc power conditions obtained from the process data have been used to investigate the effect of arc power. Table 5.1 shows the electrode conditions and calculated arc exposure.

Table 5.1. Arc exposure with a function of arc power

Case No.	Voltage (V)	Current (kA)	Power (MW)	Exposed Arc Length (inch)	Exposed Radiation Power (MW)
#1	389.1	118.3	46.0	0.00	0
#2	440.9	118.4	52.2	0.00	0
#3	478.7	123.3	59.0	0.00	0
#4	589.0	123.1	72.5	5.32	14.6
#5	653.9	130.2	85.1	8.62	23.6
#6	718.3	137.9	99.1	11.95	32.8
#7	814.6	137.9	112.3	17.94	49.2

For case #1 to #3, the electrode tip is below the top of slag layer, so that no radiation arc power is released to the freeboard. From case #4 to #7, increasing arc power leads to increasing exposed arc length, and more arc power is released to freeboard. Figure 5.7 shows the temperature distribution of the 7 cases and Figure 5.8 shows the temperature with a function of arc power. It can be read from the results that when arc power is lower than 59.0 MW, electrode tip is below slag layer, increasing arc power has little influence on side wall temperature. However, when exposed arc length is above 0, increasing arc power can significantly increase the side wall temperature. Further increase in arc power to the range above 85.1 MW could lead to WCP overheating issue.

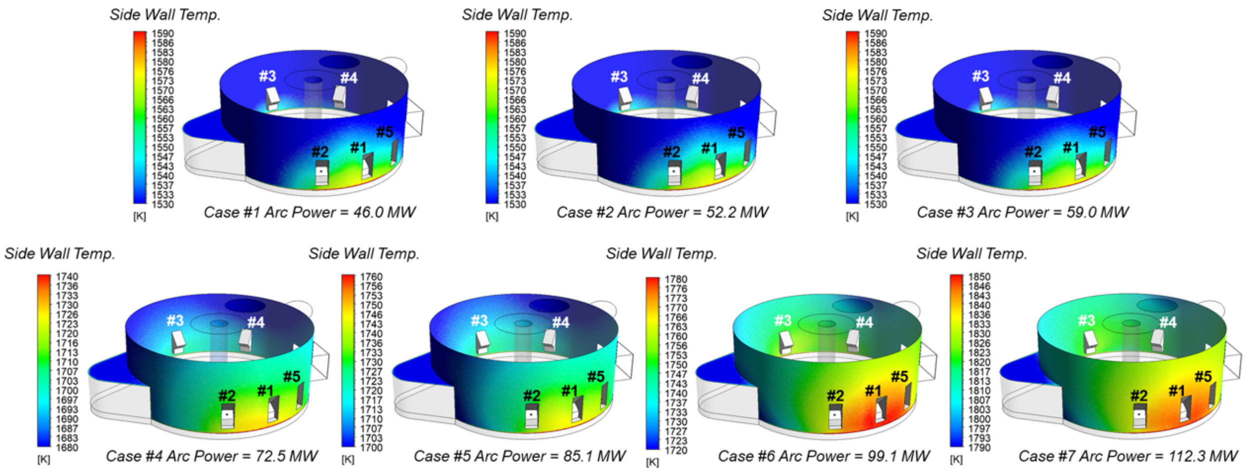

Figure 5.7. Temperature distribution with a function of arc power.

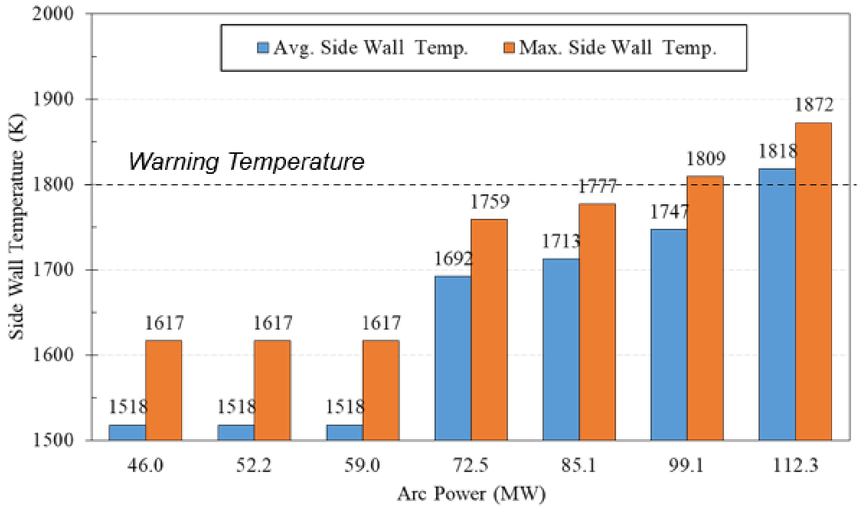

Figure 5.8. Temperature as a function of arc power.

5.3.2 Effect of Charged Scrap

In steelmaking process, the amount of charged scrap can directly determine the amount of liquid steel, furtherly can influence the slag level, which is related to the height where the post combustion is started. For example, if there is more scrap charged into the furnace, there will be more liquid steel accumulated in the molten bath. The top of liquid steel layer and slag layer, or slag level will increase. In this group of study, the electrode tip was assumed to be submerged in the slag layer. The change in the amount of charged scrap would only influence the side wall temperature through the change of the slag level. Three different scrap weights were investigated with different slag level. As shown in Table 5.2, this group of study invested 3 different input scrap weights leading to 3 different locations of slag level: 150 t, 175.8 t, and 200 t. These scraps are assumed all melted into liquid steel, and the corresponding slag levels are 13.09 inches, 9.96 inches and 7.02 inches below slag line. The side wall temperature contours are shown in Figure 5.9, maximum temperature and average temperature of side wall temperature are shown in Figure 5.10. It can be seen that the high temperature appears at the burner wall near burner #1, #2 and #5. For a higher slag level, the slag layer will be closer to the slag line, so that side wall will be more easily to be heated by the slag layer, and side wall temperature will be increased.

Table 5.2. Slag level with a function of scrap charging.

Case No.	Charged Scrap Weight (ton)	Distance below Slag line (inch)
#8	150	13.09
#9	175.8	9.96
#10	200	7.02

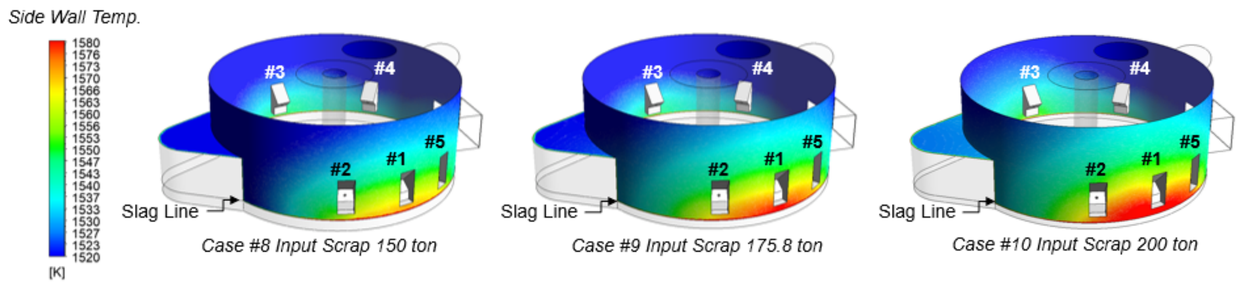

Figure 5.9. Temperature distribution as a function of slag level.

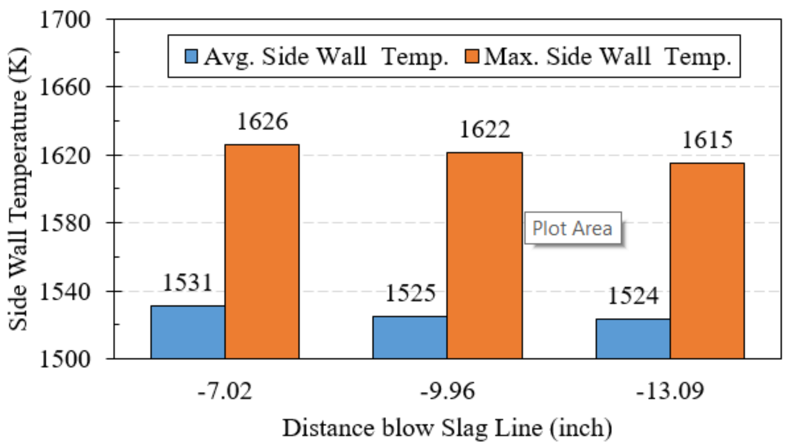

Figure 5.10. Temperature as a function of slag level.

5.3.3 Effect of Burner Condition

Burners installed on the side wall can release energy into the gas phase by combusted hot gas and the injection of oxygen jet can react with the post-combustion gas. Heat input into the gas phase in these two ways can further influence the side wall temperature distribution. This group is to investigate the influence of the burner operating conditions. Based on the case #1, two more cases with rearranged power input were simulated. The rearranged jet performance has been listed in Table 5.3. It can be seen that the amount of injected oxygen or fuel among burners are kept at the same, and the injected gas is distributed uniformly in 5 burners for case #11. In case #12, the burner #1 is turned off and the fuel and oxygen are averaged in the rest 4 burners. The simulation results have been shown in Figure 5.11 and Figure 5.12. It can be seen that for the both case with uniform burner energy input, the side wall temperature was decreased. For case #11 with uniform input gas in all 5 burners, more energy will be input at the side with 3 burners. As a result, the side wall temperature near these 3 burners will be higher. For case #12 with burner #1 turned off and the uniform power for other 4 burners, the side wall temperature distribution would be more evenly and the highest temperature would be decreased more significantly.

Table 5.3. Burner Operating Condition.

<table>
<tr><td>Case No.</td><td colspan="3">#1</td><td colspan="3">#11</td><td colspan="3">#12</td></tr>
<tr><td>Description</td><td colspan="3">Baseline (kg/s)</td><td colspan="3">5 Burners Averaged (kg/s)</td><td colspan="3">#1 Off, Rest 4 Burners Averaged (kg/s)</td></tr>
<tr><td>Burner No.</td><td>Primary O_2</td><td>Fuel</td><td>Secondary O_2</td><td>Primary O_2</td><td>Fuel</td><td>Secondary O_2</td><td>Primary O_2</td><td>Fuel</td><td>Secondary O_2</td></tr>
<tr><td>#1</td><td rowspan="3">0.857</td><td rowspan="3">0.0231</td><td rowspan="3">0.052</td><td rowspan="5">0.513</td><td rowspan="5">0.0452</td><td rowspan="5">0.185</td><td>0</td><td>0</td><td>0</td></tr>
<tr><td>#2</td><td rowspan="4">0.641</td><td rowspan="4">0.0565</td><td rowspan="4">0.232</td></tr>
<tr><td>#3</td></tr>
<tr><td>#4</td><td rowspan="2">0</td><td rowspan="2">0.0834</td><td rowspan="2">0.389</td></tr>
<tr><td>#5</td></tr>
</table>

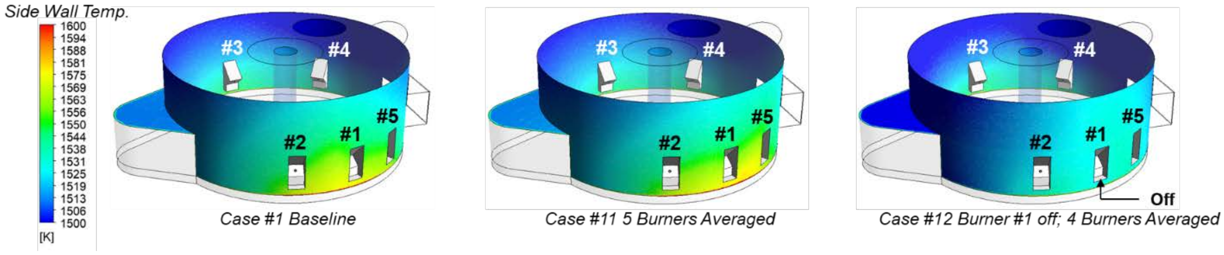

Figure 5.11. Temperature distribution as a function of burner condition.

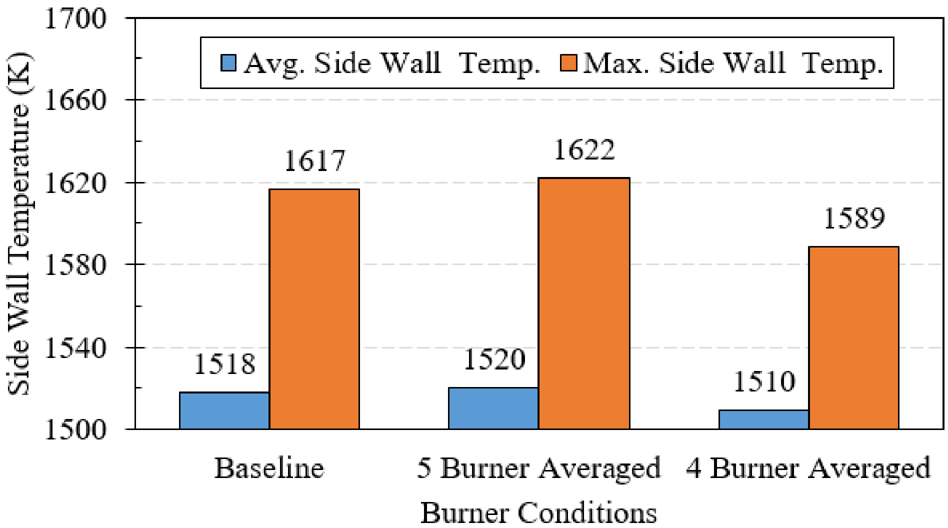

Figure 5.12. Temperature as a function of burner condition.

5.3.4 Effect of Cooling Water Flow Rate

Different cooling water flow rates were tested in this group, ie. 75% and 125%. The heat fluxes on the water-cooling panels covered walls were changed respectively, as shown in Table 5.4. The results are shown in Figure 5.13 and Figure 5.14. It can be seen that increasing the cooling water flow rate can increase the cooling rate, resulting in the side wall temperatures decrease. However, it can be not ignored that in the real operation, the time that water remaining in the cooling panel will be shorter with the increase in water flow rates. This could decrease the cooling efficiency.

Table 5.4. Wall heat flux as a function of water flow rate.

Case No.	Water Flow Rate	Water Cooling Heat Flux (kW/m^2)
#13	75%	-97.73
#1 (Baseline)	100%	-130.31
#14	125%	-162.88

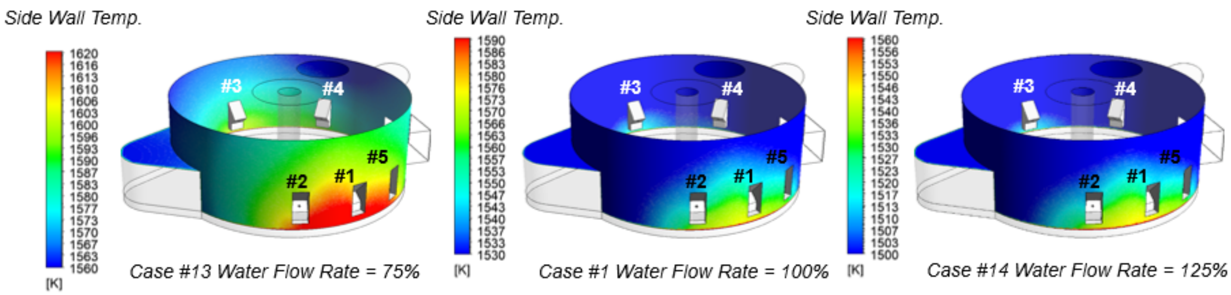

Figure 5.13. Temperature distribution as a function of water flow rate.

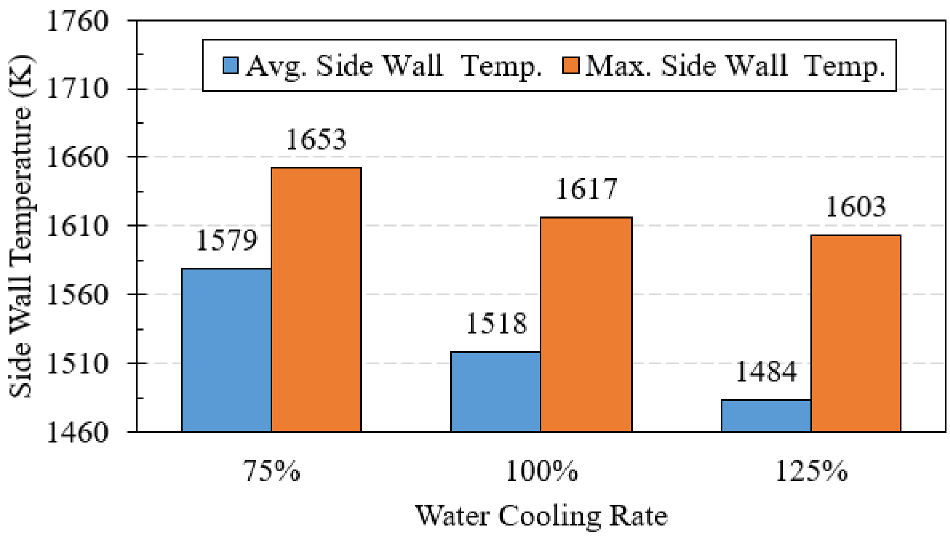

Figure 5.14. Temperature and disperse as a function of water flow rate.

5.3.5 Effect of Input Lime

In industry, high calcium lime (95% CaO) and dolomite lime (56.4% CaO, 40.6% MgO) are input to control the basicity of the slag so as to protect the refractory, since the refractory is composed by CaO and MgO. Moreover, input of CaO can help dephosphorize and desulphurize in the scrap [34]. In this project, a group of parametric studies has been conducted about the effect of the amount of input lime. The case matrix has been shown in Table 5.5. The electrode conditions are set up based on case #5, and exposed arc length has been considered in this group. In this study, it is assumed that modification of lime input will not influence the number of other species than CaO and MgO. Increasing the amount of lime will increase the components of CaO and MgO, hence viscosity will be decreased. As a result, exposed arc length will be decreased.

Table 5.5. Arc exposure with a function of lime input

Case No.	Power (MW)	Input Lime	Foaming Height (inch)	Exposed Arc Length (inch)
#15	85.1	80%	13.24	9.62
#5	85.1	100%	12.08	8.62
#16	85.1	120%	11.08	7.46

The simulation results are shown in Figure 5.15 and Figure 5.16.

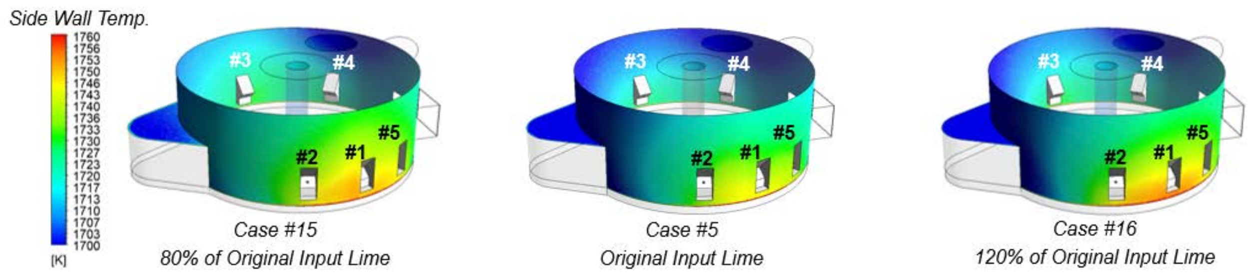

Figure 5.15. Temperature contours with a function of input lime.

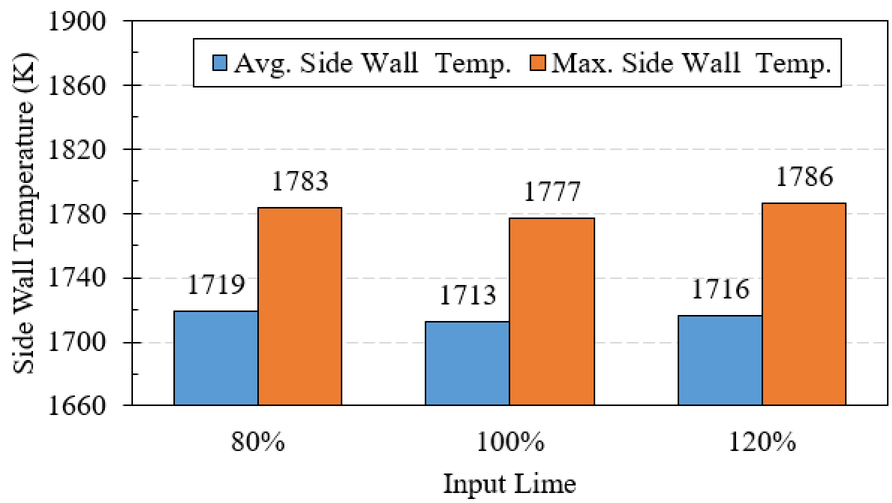

Figure 5.16. Temperature as a function of input lime.

Compare case #15 and case #5, it can be obtained that decreasing the lime input by 20% will decrease the exposed arc length, but side wall temperature is increased. This is a combined results of arc exposure and slag level. Increasing slag foaming height will lead to a higher slag level. By comparing case #5 and case #16, increasing lime input by 20% will increase exposed arc length, so that maximum side wall temperature is increased. In conclusion, it is complex for the combination effects of slag level and arc exposure.

6. ARC EXPOSURE AND SLAG FOAMING CALCULATOR

Based on the developed DC arc models, slag foaming conditions and exposed arc length can be calculated from electrode operating conditions and slag components. To visualize the calculation results by the obtained CFD results, a calculator has been developed based on the Microsoft Excel VBA to give a real-time prediction of water-cooling panel overheating issue. In this section, the calculator will be introduced using a sample case to show how it works.

As shown in Figure 6.1, when this calculator is opened, two windows can be seen. The front one is a hint window about the input parameters and output parameters. By clicking “OK” will enter the back window, the main user-interface of the calculator, as shown in Figure 6.2. This user interface contains arc mode selection, input parameters, command buttons, output parameters, and an image showing CFD results and a notification.

As a sample of industrial overheated case, DC arc mode is selected. Voltage and current are respectively 814.6 V and 137.9 kA. The sample slag in Table 3.4 is used for this calculation. Click “Calculate” and the calculation results can be obtained, as shown in Figure 6.3. Calculation of share of arc power is disabled in DC arc mode. Total arc length and slag foaming can be calculated from electrode condition and slag components, then exposed arc length can be calculated according to these two parameters. The “Image” part shows the arc channel status and side wall temperature distribution. The side wall temperature distribution is obtained from the pre-run simulation results. The “Notification” will show whether this case may suffer water-cooling panel overheating issue according to the computational results of exposed arc length. In this sample, overheating issue may take place.

If the input parameters are modified, calculation results will be changed accordingly. As shown in Figure 6.4, the voltage is reduced to 600 V, the total arc length will be reduced to 17.1 inch, and exposed arc length reduced to 5.01 inch. The relative image shows a reduced side wall temperature distribution and arc channel, the notification shows there is no risk of overheating issue in this case.

Further one more trial, if the slag composition is changed, the calculator will change the foaming height to change the exposed arc length. As shown in Figure 6.5, 7 % less CaO and 7% more SiO_2 are considered in this case. This modification increases the viscosity and the final foaming height is increased to a term that totally covers the exposed arc. It can be noticed that there will be no arc channel in this case, and the side wall temperature is furtherly decreased. Obviously, this further cooled down case will have no risk about water-cooling panel overheating issue.

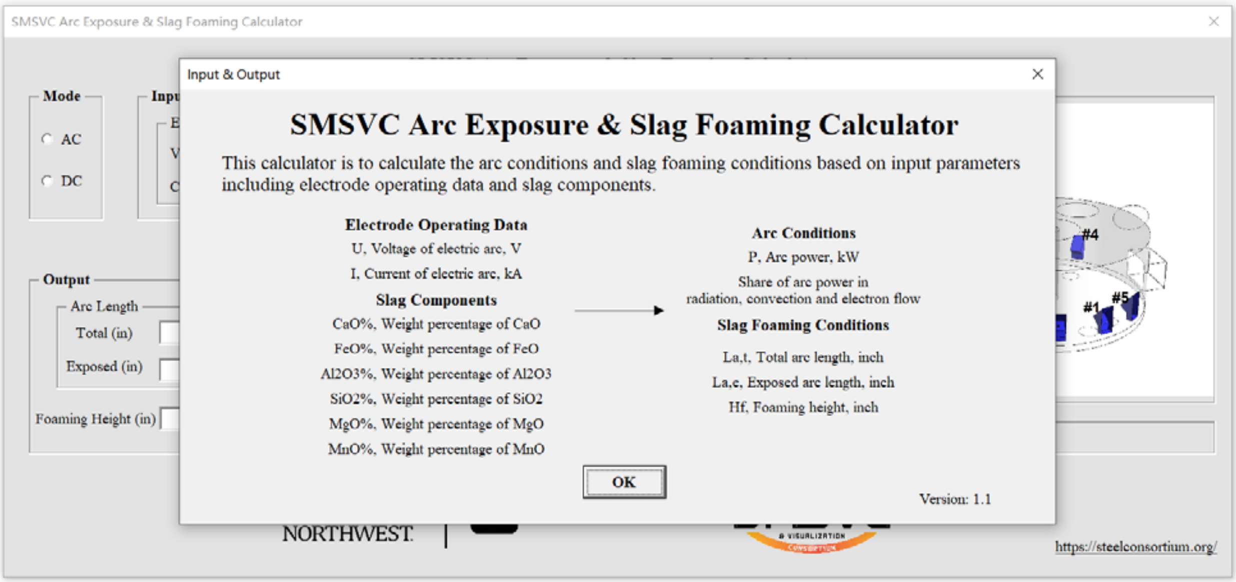

Figure 6.1 Hint window about input and output parameters.

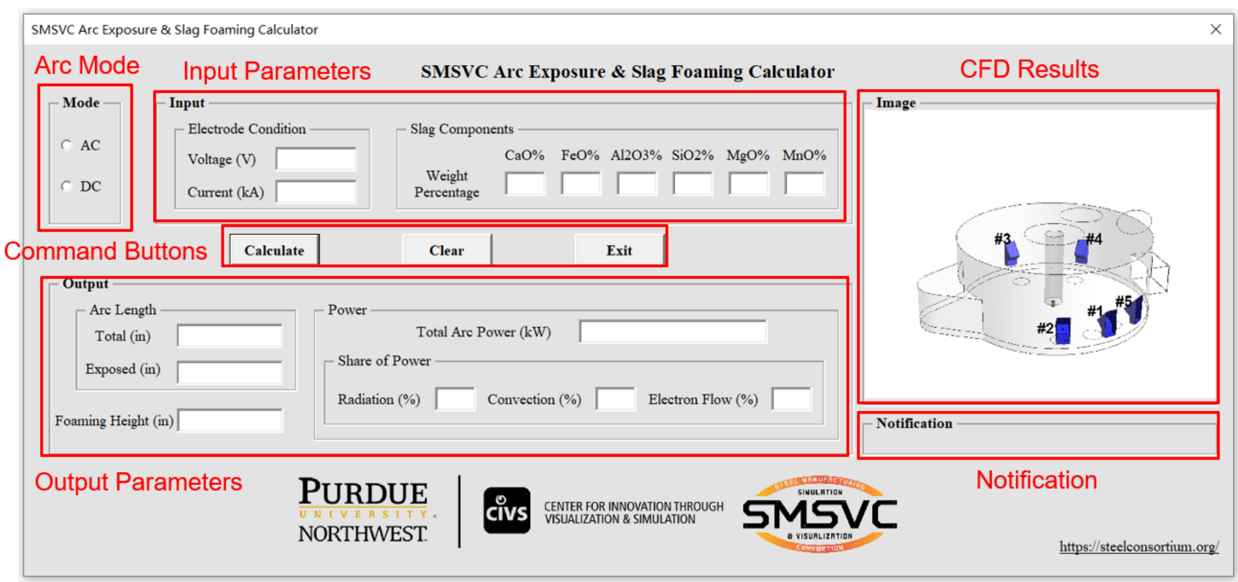

Figure 6.2 User interface of the arc exposure and slag foaming calculator.

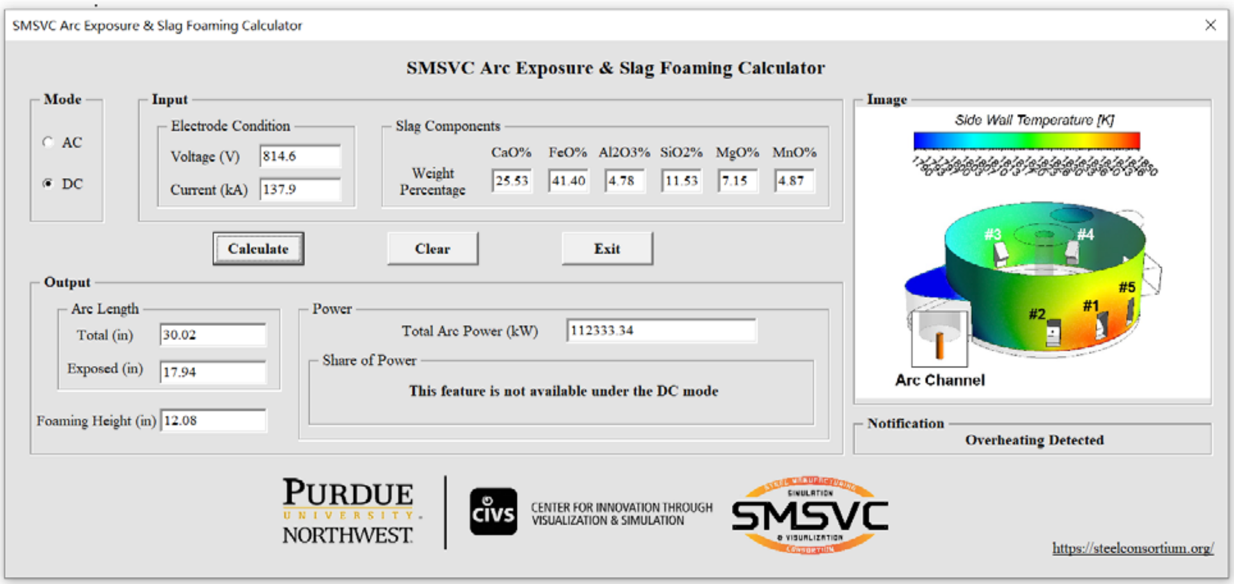

Figure 6.3 A sample case for the calculator.

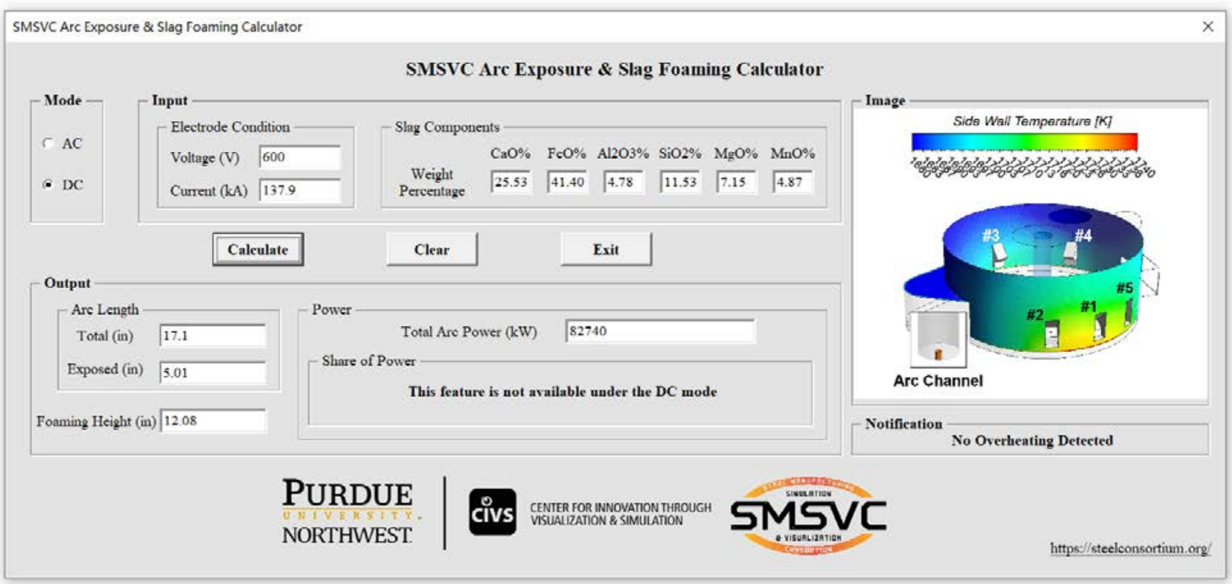

Figure 6.4 Modified voltage of the sample case.

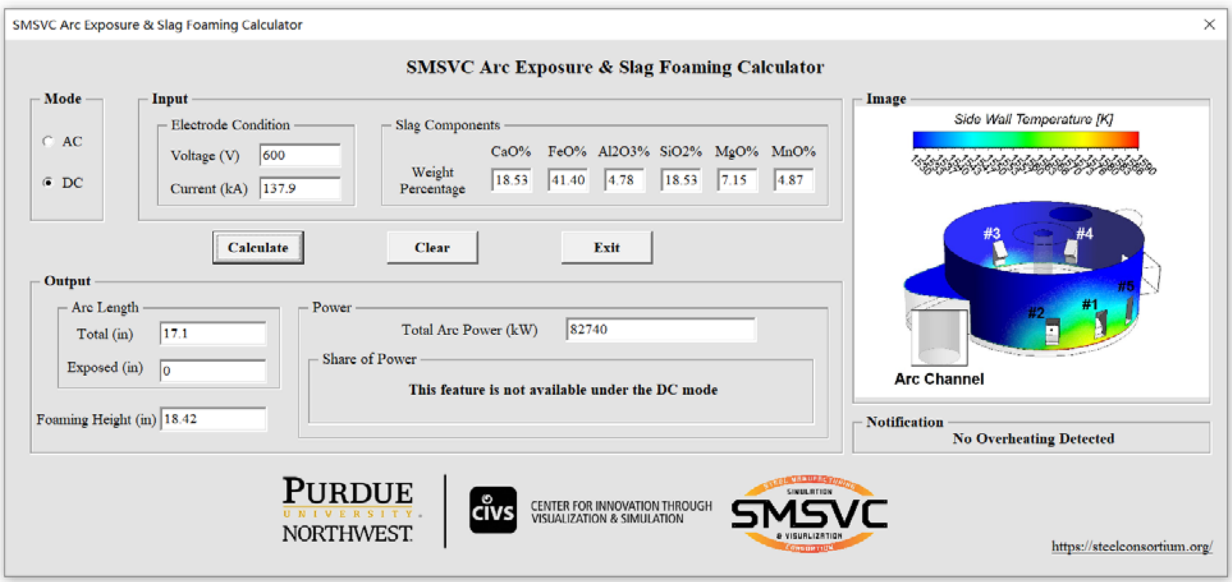

Figure 6.5 Modified voltage and slag components of the sample case.

7. CONCLUSIONS

A slag foaming model composed by series of DC arc models has been developed to calculate the relative parameters of arc exposure and slag foaming according to electrode operating condition and slag compositions. The calculated results could be the input of the CFD simulator.

A 3D freeboard simulator has been applied to solve the water-cooling panel overheating issue in SSAB. The results show that the unbalanced burner power input from both sides of the furnace is the key to cause the non-uniformity of side wall temperature distribution, and the local overheating is detected in the region near burner #1, #2, #5, and the main cause to elevate overall side wall temperature and intensify the local overheating issue is from the excessive arc exposure.

A calculator has been generated with combined slag foaming model and CFD results to visualize the calculation results so as to give a real time control of the water-cooling panel overheating issue.

To reduce the local overheating issue due to burner operations, the bath/slag level needs to be decreased and burner #1 needs to be off. To reduce the overall side wall temperature, the slag foaming as well as the water flow rate need to be increased.

REFERENCES

1. World Steel Association, *Steel Statistical Yearbook 2020: concise version*, Brussels, Belgium, November 2019
2. Tolomeo, N., M. Fitzgerald, and J. Eckelman. "US Steel Sector Thrives as Mills Move up Quality Ladder." *S&P Global Platts Insight* (2019).
3. Liu, Han-qiao, Guo-xia Wei, Hui-hua Ye, and Shu-guang Zhang. "Characteristics of Molten Slag from Hospital Waste Incineration Ash by Electric Arc Furnace." *In 2009 International Conference on Energy and Environment Technology*, vol. 3, pp. 226-229. IEEE, 2009.
4. Odenthal, Hans-Jürgen, Andreas Kemminger, Fabian Krause, Lukas Sankowski, Norbert Uebber, and Norbert Vogl. "Review on modeling and simulation of the electric arc furnace (EAF)." *steel research international* 89, no. 1 (2018): 1700098.
5. Alam, Morshed, Jamal Naser, Geoffrey Brooks, and Andrea Fontana. "Computational fluid dynamics modeling of supersonic coherent jets for electric arc furnace steelmaking process." *Metallurgical and Materials Transactions B* 41, no. 6 (2010): 1354-1367.
6. Matsuura, Hiroyuki, Christopher P. Manning, Raimundo AFO Fortes, and Richard J. Fruehan. "Development of a decarburization and slag formation model for the electric arc furnace." *ISIJ international* 48, no. 9 (2008): 1197-1205.
7. Luz, A. P., T. A. Ávila, P. Bonadia, and V. C. Pandolfelli. "Slag foaming: fundamentals, experimental evaluation and application in the steelmaking industry." Refractory Worldforum 3, no. 2 (2011): 91-98.
8. Opitz, Florian, Peter Treffinger, and Jürgen Wöllenstein. “Modeling of Radiative Heat Transfer in an Electric Arc Furnace.” *Metallurgical and Materials Transactions B* 48, no. 6 (2017) Pages 3301-3315.
9. Chen, Yuchao. "Numerical Modeling of Supersonic Coherent Jet and In-Bath Multiphase Flow Behavior During the Steel Making Process in the Electric Arc Furnace." PhD diss., Purdue University, 2018.
10. Tang, Guangwu, Yuchao Chen, Armin K. Silaen, Yury Krotov, Michael F. Riley, and Chenn Q. Zhou. "Effects of fuel input on coherent jet length at various ambient temperatures." *Applied Thermal Engineering* 153 (2019): 513-523.

11. Chen, Yuchao, Armin K. Silaen, and Chenn Q. Zhou. "3D integrated modeling of supersonic coherent jet penetration and decarburization in EAF refining process." *Processes* 8, no. 6 (2020): 700.
12. Jones, R. T., Q. G. Reynolds, and M. J. Alport. "DC arc photography and modelling." *Minerals Engineering* 15, no. 11 (2002): 985-991.
13. Bowman, Ben. "Properties of arcs in DC furnaces." *In 52nd Electric Furnace Conference*, pp. 111-120. 1994.
14. Ito, Kimihisa, and R. J. Fruehan. "Study on the foaming of CaO-SiO 2-FeO slags: Part I. Foaming parameters and experimental results." *Metallurgical transactions B* 20, no. 4 (1989): 509-514.
15. Ito, Kimihisa, and R. J. Fruehan. "Study on the foaming of CaO-SiO 2-FeO slags: Part II. Dimensional analysis and foaming in iron and steelmaking processes." *Metallurgical Transactions B* 20, no. 4 (1989): 515-521.
16. Jiang, R., and R. J. Fruehan. "Slag foaming in bath smelting." *Metallurgical transactions B* 22, no. 4 (1991): 481-489.
17. Zhang, Y., and R. J. Fruehan. "Effect of the bubble size and chemical reactions on slag foaming." *Metallurgical and materials transactions B* 26, no. 4 (1995): 803-812.
18. Wu, L. S., Galina Jelkina Albertsson, and Du Sichen. "Modelling of slag foaming." *Ironmaking & steelmaking* 37, no. 8 (2010): 612-619.
19. Matsuura, Hiroyuki, Christopher P. Manning, Raimundo AFO Fortes, and Richard J. Fruehan. "Development of a decarburization and slag formation model for the electric arc furnace." *ISIJ international* 48, no. 9 (2008): 1197-1205.
20. Khodabandeh, Erfan, Mohsen Ghaderi, Abolfazl Afzalabadi, Abel Rouboa, and Amir Salarifard. "Parametric study of heat transfer in an electric arc furnace and cooling system." *Applied Thermal Engineering* 123 (2017): 1190-1200.
21. Mombeni, Afshin Gharib, Ebrahim Hajidavalloo, and Morteza Behbahani-Nejad. "Transient simulation of conjugate heat transfer in the roof cooling panel of an electric arc furnace." *Applied Thermal Engineering* 98 (2016): 80-87.
22. Sanchez, JLG, Conejo AN, and Ramirez-Argaez MA. "Effect of foamy slag height on hot spots formation inside the electric arc furnace based on a radiation model." *ISIJ international* 52, no. 5 (2012): 804-813.

23. Gruber, Jacqueline C., Thomas Echterhof, and Herbert Pfeifer. "Investigation on the influence of the arc region on heat and mass transport in an EAF freeboard using numerical modeling." *Steel research international* 87, no. 1 (2016): 15-28.
24. Yigit, Cemil, Gokhan Coskun, Ekrem Buyukkaya, Ufuk Durmaz, and Hasan R. Güven. "CFD modeling of carbon combustion and electrode radiation in an electric arc furnace." *Applied Thermal Engineering* 90 (2015): 831-837.
25. Scheepers, Emile, Yongxiang Yang, Allert T. Adema, Rob Boom, and Markus A. Reuter. "Process modeling and optimization of a submerged arc furnace for phosphorus production." *Metallurgical and Materials Transactions B* 41, no. 5 (2010): 990-1005.
26. Siegel, R. H. J. R., and John R. Howell. "Thermal radiation heat transfer, Hemisphere Pub." *Corp., Washing ton DC* (1992).
27. Alexis, Jonas, Marco Ramirez, Gerardo Trapaga, and Pär Jönsson. "Modeling of a DC electric arc furnace—heat transfer from the arc." *ISIJ international* 40, no. 11 (2000): 1089-1097.
28. Guo D., and Irons G.A. *Third International Conference on CFD in the minerals and process industries*, Melbourne. Australia, (2003), pp. 223–28.
29. MacRosty, Richard DM, and Christopher LE Swartz. "Dynamic modeling of an industrial electric arc furnace." *Industrial & engineering chemistry research* 44, no. 21 (2005): 8067-8083.
30. Bowman, Ben, and Klaus Krüger. *Arc furnace physics*. Düsseldorf: Verlag Stahleisen, 2009.
31. Logar, Vito, Dejan Dovžan, and Igor Škrjanc. "Modeling and validation of an electric arc furnace: Part 1, heat and mass transfer." *ISIJ international* 52, no. 3 (2012): 402-412.
32. Wu, Chengchuan, Guoguang Cheng, and Qiqi Ma. "Calculating Models on the Surface Tension of CaO-FeO-SiO2 Molten Slags." *Research of Materials Science* 3, no. 1 (2014).
33. Xuan, Changji, Hiroyuki Shibata, Sohei Sukenaga, Pär Göran Jönsson, and Keiji Nakajima. "Wettability of Al2O3, MgO and Ti2O3 by liquid iron and steel." *Isij International* 55, no. 9 (2015): 1882-1890.
34. Pretorius, Eugene B., and Robert C. Carlisle. "Foamy slag fundamentals and their practical application to electric furnace steelmaking." *Iron & steelmaker* 26, no. 10 (1999): 79-88.
35. Mills. Ken. "The estimation of slag properties." *Southern African Pyrometallurgy* 7, no. 3 (2011): 35-42.

36. Riboud, P. V., RIBOUD PV, and LUCAS LD. "Improvement of continuous casting powders." (1981).
37. Urbain, G. “Viscosity estimation of slags”. *Steel Res* 58 (1987) 111/116.
38. Iida, Takamichi, Hidenori Sakai, Yoshifumi Kita, and Katsuhiko Murakami. "Equation for estimating viscosities of industrial mold fluxes." *High Temperature Materials and Processes* 19, no. 3-4 (2000): 153-164.
39. Itoh, Satoshi, Akira Tsubone, Kazuyo Matsubae-Yokoyama, Kenichi Nakajima, and Tetsuya Nagasaka. "New EAF dust treatment process with the aid of strong magnetic field." *ISIJ international* 48, no. 10 (2008): 1339-1344.
40. Mills, K. C., and S. Sridhar. "Viscosities of ironmaking and steelmaking slags." *Ironmaking & Steelmaking* 26, no. 4 (1999): 262-268.